

pubs.acs.org/cm Perspective

When Assembly Meets Processing: Tuning Multiscale Morphology of Printed Conjugated Polymers for Controlled Charge Transport

Kyung Sun Park," Justin J. Kwok," Prapti Kafle," and Ying Diao*



Cite This: *Chem. Mater.* 2021, 33, 469–498

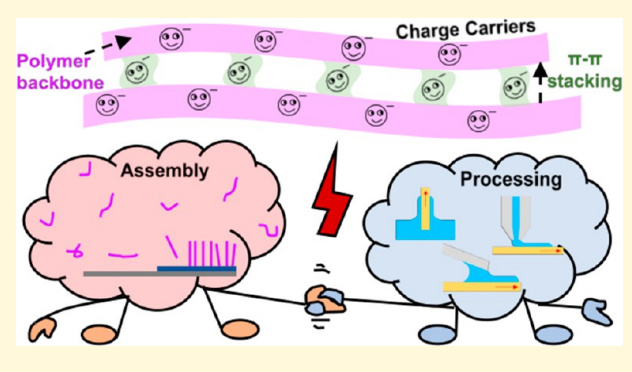


ACCESS

Metrics & More

Article Recommendations

ABSTRACT: Conjugated polymers are rapidly emerging as an attractive class of semiconductors for next-generation electronics thanks to their low-cost, high-throughput solution processability, mechanical flexibility, stretchability, self-healing properties, and ability to interface and communicate with biological systems. Accordingly, the last four decades has seen a surge of studies that have provided seminal contributions to the thorough understanding of conjugated polymers. One of the key factors that dictates the electronic performance of conjugated polymers is their assembly and crystallization behavior, which has remained intriguing and challenging to study. The complex solution processing environment and rapid kinetics strongly couple with the conjugated polymer assembly



process, further complicating a full mechanistic picture. In this perspective, we summarize the charge transport mechanism, fundamentals of conjugated polymer assembly, and solution printing. We further discuss central strategies that have been developed to control and enhance their multiscale assembly during solution printing. Finally, we hope that our perspective will stimulate more studies on how processing can control morphology and charge transport of conjugated polymers and applications of these concepts to other advanced functional materials.

1. INTRODUCTION

The discovery of the first conducting polymer, chemically doped polyacetylene, in 1977 gave birth to a new field of chemistry and a paradigm shift ensued in the way we view electrically active materials. Thenceforth, conjugated polymers have rapidly emerged as a new class of organic semiconductors, setting out to renew the semiconducting industry that has been dominated by inorganic materials like silicon for the past five decades. The overwhelming interest in organic semiconductors stems in part from the fact that, contrary to inorganic materials that require demanding processing conditions such as high temperature and high vacuum, these materials can be solutionprocessed under near-ambient conditions, while sometimes demonstrating optoelectronics properties on par with inorganic materials. Conjugated polymers, in particular, provide additional advantages as they enable fabrication of large area uniform films. Their molecular structure can also be easily engineered to tune solubility and solution rheological properties, which significantly impacts solution processing. These advantages ultimately facilitate the fabrication of inexpensive, lightweight, flexible, stretchable, and biointegratable devices.²⁻⁴

Inorganic and organic semiconductors exhibit distinct charge transport mechanisms. The constituent atoms in

inorganic semiconductors are held together by strong covalent bonds, resulting in highly ordered crystalline structure. In contrast, organic semiconductors have weak dispersive interactions between the molecular constituents, making them highly susceptible to structural disorders. Theoretical and experimental studies dedicated to elucidating charge transport mechanisms in solid materials have shown that depending on the degree of order, charge transport could occur in two opposing regimes: itinerant band-like transport, localized hopping, or an intermediate characteristic between the two.⁵ In highly crystalline solids, such as common inorganic materials and highly purified molecular single crystals, band-like transport of charge carriers dominates. Here, highly ordered packing of the entities in the crystal lattice results in full delocalization of the charge carriers in band edges; the charge carriers have an unhindered path until they reach scattering centers or phonons, which are intermolecular vibrations of the crystal lattice.6 Under the

Received: October 25, 2020 Revised: December 18, 2020 Published: January 13, 2021





[†]This Perspective is part of the *Up-and-Coming* series.

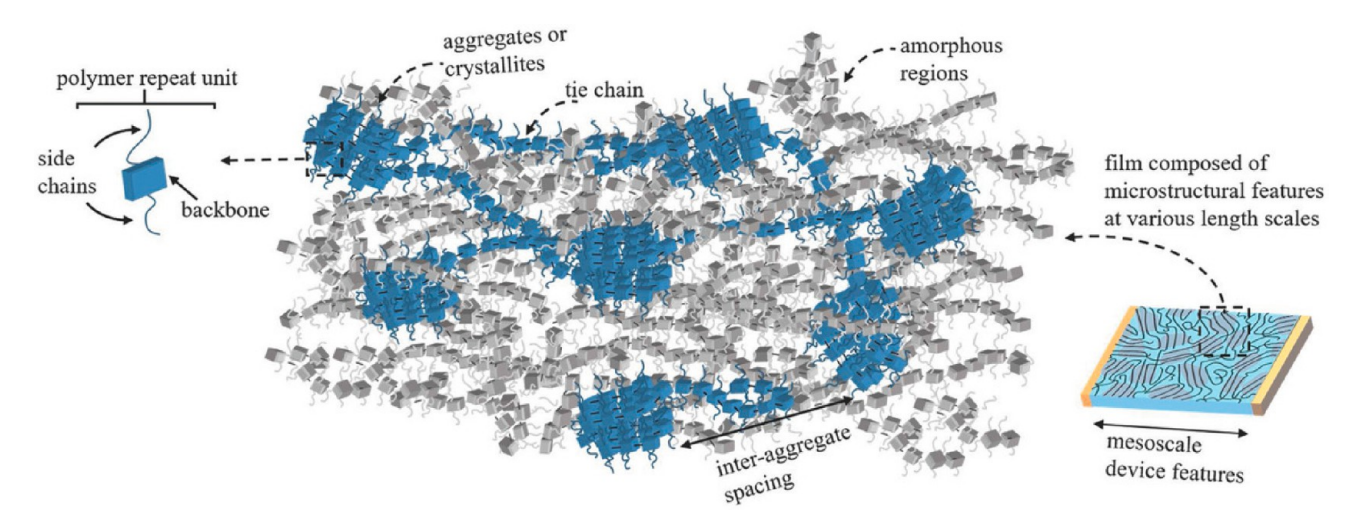


Figure 1. Cartoon representation of the hierarchical structure of conjugated polymers that determines charge transport at multiple length scales. Starting from a few nanometers to tens of hundreds of nanometers, features such as polymer conformation, crystallinity, and polymer alignment dictate the charge transfer process. At mesoscale dimension on par with the size of a typical device, the charge transport is limited by connectivity of the crystalline domains within amorphous regions by tie chains. Reproduced with permission from ref 25. Copyright 2018 John Wiley and Sons.

influence of an electric field, the charge carriers experience a Coulombic force, leading to a net displacement at a velocity proportional to the applied field with the proportionality constant being mobility. In these systems, the mobility decreases with an increase in temperature because of the increase in phonon concentration. In contrast, charge transport in organic semiconductors, which are relatively disordered, is largely influenced by both molecular and crystalline properties. The small overlap of molecular orbitals stemming from weak van der Waals interactions and the consequent creation of disorders ultimately results in localization of charges.⁶ During the characteristic residence time scale, the charge carriers polarize the surrounding electronic and nuclear subsystems. The charge carriers along with the polarized electron cloud then creates polarons, which exhibit higher effective mass and decreased mobility as compared to the charge carriers alone. In addition, molecular systems are infirmed with disorders: (i) static disorders arising from structural defects in the crystal or chemical impurities that act as charge traps; (ii) dynamic disorder stemming from coupling of charge carriers with lattice vibrations, i.e., phonons (caused by thermal fluctuation), that results in the fluctuation of the charge transfer integral. As a result, charge transport in organic semiconductors usually does not follow a band-like mechanism at ambient conditions. In weakly disordered molecular solids, e.g., organic small molecule polycrystals, charge transport is described by the multiple trap and release model where barriers such as grain boundaries result in trapping and detrapping of charge carriers. This model assumes a distribution of localized energy levels in the vicinity of a delocalized transport band; as the charge carriers arrive at the localized states, they are trapped instantaneously while their release is thermally

The charge transport mechanism for conjugated polymers is distinct from that of organic small molecules because of their unique molecular structures, where π -electrons are delocalized along the polymer backbones in addition to between cofacially stacked chains. Moreover, conjugated polymers adopt hierarchical structures from conformation of single polymer chains, packing in polymer aggregates to the network architecture of polymer aggregates, leading to different

mechanisms of charge transport at different length scales (Figure 1). 10 At a distance of a few nanometers, on par with the persistence length of conjugated polymers, the charge carriers can ideally move freely along the polymer backbone. The conjugation of unhybridized p_x carbon orbitals along a single polymer chain forms extended π -orbitals, providing a pathway for intrachain charge transport. 11 Thus, charge transport is limited by intrachain electronic coupling which is greatly affected by polymer chain conformation. 12 Polymers that are more flexible or have higher backbone torsional angles have increased conformational disorder and decreased effective conjugation length. 13,14 In this scenario, the charge transport is modeled by incoherent hopping where charge carriers hop from one localized state to another.⁶ The charge carrier mobility is much lower in hopping transport compared to band transport and is also thermally activated; hence, the mobility increases with temperature. Although hopping transport is expected for typical conjugated polymer systems, recent studies¹⁵⁻¹⁸ have shown that band-like transport is also feasible in conjugated polymers. Apart from the high degree of crystallinity and alignment, the polymers used in most of these studies were designed to have high backbone planarity and exhibited low trap density. When individual polymer chains interact to form aggregates or crystallites (tens of nanometers), the π -orbitals of neighboring chains are cofacially stacked, providing a pathway for interchain charge transport. Within these ordered regions, charge transport is limited by interchain hopping events which is a couple of magnitudes slower than intrachain hopping. The charge carrier mobility at this length scale can be enhanced by increasing the extent of electronic coupling between the polymer chains accomplished by utilizing either polymer synthesis or processing methods so that the polymers pack with closer π - π distance and form larger aggregates or crystallites. In addition, alignment of polymer chains is extremely beneficial as it reduces the frequency of interchain charge hopping which is slower and energetically more demanding than intrachain transport.¹⁹ At a length scale larger than the size of crystallites/aggregates (hundreds of nanometers and above), the transport is dictated by the hopping events between aggregates/crystallites. Owing to high degrees of conformational freedom and thus sluggish

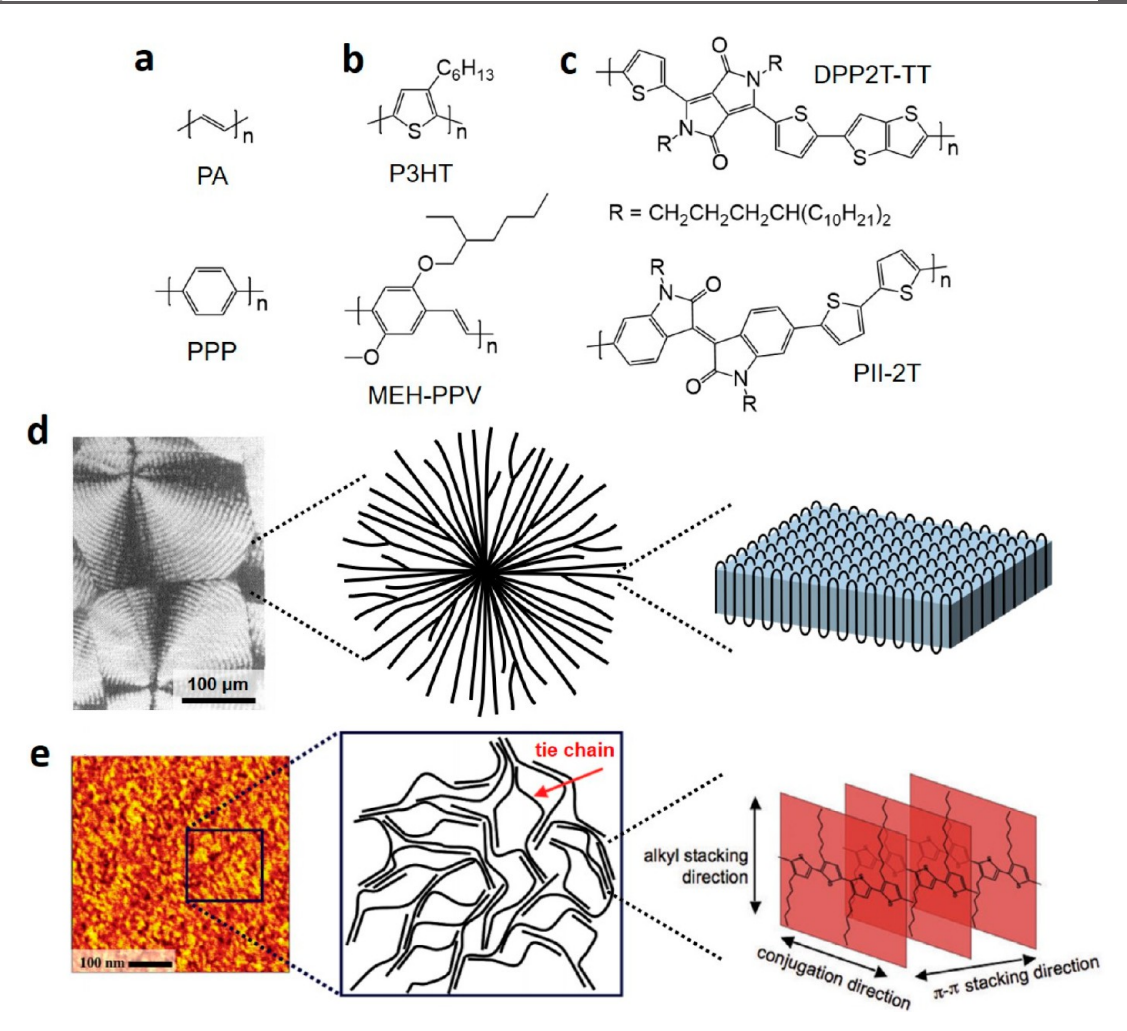


Figure 2. Morphology of flexible vs conjugated polymer crystallites and the molecular structure of three generations of conjugated polymers. Examples of conjugated polymers: (a) first generation, polyacetylene (PA) and polyparaphenylene (PPP), (b) second generation, P3HT and poly[2-methoxy-5-(2-ethylhexyloxy)-1,4-phenylenevinylene] (MEH-PPV), and (c) third generation, diketopyrrolopyrrole-based (DPP2T-TT) and isoindigo-based (PII-2T) conjugated polymers. (d) Cross-polarized optical microscopy (CPOM) image of polyethylene spherulite (left) and schematic of spherulite structure (middle) composed of lamellae (right). (left) Reproduced with permission from ref 41. Copyright 1982 John Wiley & Sons, Inc. (e) Atomic force microscopy (AFM) image of P3HT film (left), schematic of molecular structure consisting of locally ordered regions bridged by tie chains (middle), and schematic of the crystal structure of P3HT. (left and middle) Reproduced with permission from ref 42. Copyright 2005 American Chemical Society. (right) Reproduced with permission from ref 11. Copyright 2007 Elsevier Ltd.

crystallization, conjugated polymers often have crystalline regions connected by amorphous regions. The electronic properties, such as bandgap, of amorphous regions are usually distinct from those of crystalline regions causing it to be energetically expensive for charges to move across the order/ disorder interface.²⁰ Moreover, lack of π -orbital overlap between polymer chains hinders charge transport in amorphous regions. In this regard, polymer chains without kinks that link crystalline regions, or tie-chains, have been recognized as essential for charge transport in semicrystalline polymer thin films.²⁰ Here, kink refers to the position in a polymer chain where the tangent vector becomes perpendicular to the field direction.²¹ In particular, Mollinger and Spakowitz et al. have recognized that the persistence length of the polymers should be sufficiently long to bridge the distance between the crystallites to achieve continuous charge transport through tie chains.²¹ Recently, Gu and Loo et al. have identified the importance of a critical tie-chain fraction required for efficient transport.²² Utilizing the Huang-Brown model,^{23,24} they found that the critical tie-chain fraction for poly(3-hexylthiophene) (P3HT) is 10^{-3} . The charge transport below the critical fraction was limited by connectivity between crystallites, while above the critical fraction, it was determined by the disorder within the crystallites.

The multiscale morphology of conjugated polymers crucially influences charge transport. Starting from the conformation of a single polymer chain, factors such as the spacing between the polymer chains in aggregates, as well as the size, alignment, and interconnectivity of aggregates, ultimately dictate the fate of charge carriers in the polymers. The time scale of polymer assembly into highly ordered structures is usually slower than the polymer processing time scale. In other words, the polymeric system usually fails to reach equilibrium during processing, making it difficult to attain the desirable ordering from backbone planarization, high degree of crystallinity, and percolation pathways between crystallites, to alignment of aggregates. To that end, tremendous research efforts from designing molecules to innovating processing have been made by the community to direct hierarchical self-assembly at different length scales. In this perspective, we review

fundamentals of polymer crystallization and assembly as well as recent advances on various solution processing techniques and strategies that have been developed to improve and control charge transport.

FUNDAMENTALS OF POLYMER CRYSTALLIZATION AND ASSEMBLY

2.1. Thermodynamics (and Kinetics) of Polymer Crystallization. To precisely control the multiscale morphology of conjugated polymer thin films it is important to understand polymer nucleation and growth and the multiscale assembly process that ensues. However, due to complex behavior, there is currently no widely accepted fundamental theory for conjugated polymer nucleation and growth. Instead, here we will briefly summarize the fundamentals of polymer nucleation and growth that were developed for flexible polymers. We will then discuss how differences between flexible and conjugated polymers such as side chains and backbone stiffness lead to observed changes in crystallization behavior.

It is widely accepted that flexible polymer chains crystallize by undergoing chain folding to form lamellae which can then form single crystals or spherulites (Figure 2d). This was observed as early as 1938²⁶ but was not accepted until the 1960s when most notably Keller and co-workers²⁷ provided evidence of chain folding in polyethylene crystals and others began to show that the previously accepted fringed micelle model was unsuitable.²⁸ Several theories have now been developed to describe the polymer crystallization process which is a kinetic process since polymer crystals are frequently found to be in metastable states. While the exact details of how chain folding and subsequent crystallization takes place varies between theories, a simple starting point is the Hoffman-Lauritzen (HL) theory.²⁹ HL theory describes polymer crystallization using thermodynamics and kinetics of polymer surface nucleation and growth. As is typical for kinetic theories, it is based upon a nucleation barrier arising from the competition between bulk free energy and surface free energy. As it is a secondary nucleation theory, the crystallization process first starts with nucleation of chain folded segments, or "stems", onto an existing surface. Afterward, stems can either continue to deposit and grow to form a new layer parallel to the surface (lateral growth), or they can nucleate onto the new layer perpendicular to the surface. The competition between the surface nucleation and lateral growth gives rise to three growth regimes. As a result, HL theory was able to describe spherulite growth and understand its dependence on parameters such as undercooling and lamellae size. Many subsequent theories have built upon HL to account for more complexity and considerations.³⁰

Compared to flexible polymers like polyethylene, conjugated polymers exhibit distinct molecular structures and crystallite morphology. The defining feature of conjugated polymers is the alternating C=C bond along the polymer chain's backbone which delocalizes π -electrons. This general molecular structure can be clearly seen in examples of first generation conjugated polymers ³¹ (Figure 2a) such as polyacetylene which has a linear structure or in polyparaphenylene which consists of an aromatic structure. The conjugation enhances the rigidity of the polymer due to the enhanced π - π interactions along the backbone. In fact, earlier studies on conjugated polymers frequently referred to them as rod-like or rigid rod polymers. ³²⁻³⁷ The second generation of conjugated

polymers is characterized by enhanced solubility and processability, generally through the addition of side chains to the conjugated backbone (Figure 2b). The most well-known example of this is P3HT which contains alkyl side chains. Side chain engineering is a topic still currently being studied which has implications beyond just improving solubility but also changing polymer conformation, morphology, and functionality. Current state-of-the-art, third generation conjugated polymers have more complex molecular structures and typically consist of alternating conjugated moieties which are electron donors and electron acceptors (Figure 2c). These are referred to as donor-acceptor (D-A) conjugated polymers and exhibit enhanced electronic properties due to further delocalization of electrons along the backbone. A consequence of typical D-A molecular structure is that these conjugated polymers are found to be highly rigid.³⁸ The rigidity could potentially be further enhanced by designing conjugated ladder polymers where all the backbone units are fully fused and π conjugated.³⁹ At this point it can be seen that conjugated polymers exhibit complex intramolecular and intermolecular assembly behavior as a result of their unique molecular design which imparts stiffness and side chain effects. The question is then whether or not polymer crystallization theory developed for flexible polymers is appropriate for conjugated polymer crystallization. For relatively flexible conjugated polymers, such as P3HT, chain folding does indeed occur and in specific cases can form spherulites although fibril-like aggregates are still typically formed.⁴⁰ However, for first generation conjugated polymers which lacked side chains and the third generation conjugated polymers with large donor-acceptor conjugated cores, the formation of chain-folded lamellae does not occur due in part to increased rigidity (discussed in detail below). Instead, fibril-like aggregation and networks are common. A typical morphology is shown in Figure 2e for P3HT which is semicrystalline, consisting of locally ordered regions bridged by tie chains.

Currently, there is no well-established fundamental theory for conjugated polymer crystallization. The majority of work on conjugated polymers has instead largely focused on tuning molecular structure or developing processing methods and observing changes in thin film morphology. Therefore, we will discuss primarily the effect of how polymer stiffness and side chains affect the polymer crystallization or assembly. While conjugated polymers are assumed to be rigid, actual measurements of persistence are not commonly reported except for a few of the most commonly studied conjugated polymers such as P3HT. In addition, while relatively rigid compared to flexible polymers like polyethylene, conjugated polymers vary in their stiffness. For example, conjugated homopolymers are presumably more flexible compared to D-A conjugated polymers. For reference, polyethylene has a persistence length of 0.7 nm whereas P3HT has a persistence length of ~2.8 nm.³⁸ The persistence length can be determined experimentally with techniques such as small-angle X-ray/neutron scattering (SAXS/SANS), static light scattering, and intrinsic viscosity measurement or computationally using density functional theory and molecular dynamics simulations. First generation conjugated polymers exhibited poor solubility making reports of persistence length somewhat uncommon, although sometimes reported to be ~10 nm or several tens of nanometers. 43 Second generation conjugated polymers typically have persistence lengths of ~2-10 nm while third generation conjugated polymers, such as the modern D-A

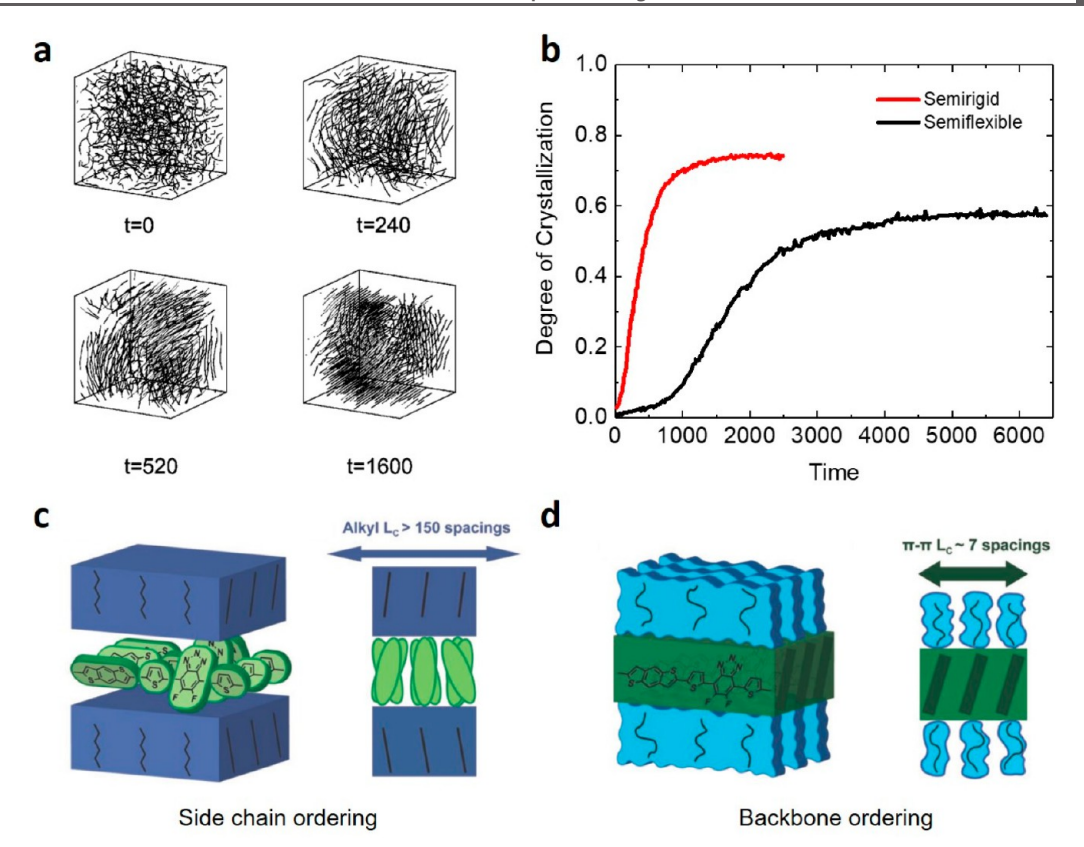


Figure 3. Examples of rigidity and side chain effect on crystallization process. (a) Simulated melt crystallization process of a semirigid chain and (b) degree of crystallization comparing semirigid and semiflexible chains. (a, b) Adapted with permission from ref 45. Copyright 2001 American Physical Society. (c) Side chain ordering with disordered torsional backbone and (d) backbone ordering with disordered side chains. (c, d) Reproduced with permission from ref 52. Copyright 2018 Wiley-VCH Verlag GmbH & Co. KGaA, Weinheim.

conjugated polymers, are estimated to have persistence lengths ranging from ~10 nm to several tens of nanometers.³⁸ Chain folding in P3HT has been directly observed by scanning tunneling microscope (STM)⁴⁴ as well as inferred from the orientation of the backbone along the short, radial direction of nanofibers. However, chain folding has not been observed for D-A conjugated polymers which is consistent with their presumably higher degree of rigidity. Instead D-A conjugated polymers tend to aggregate or crystallize into nanofibers with the conjugated backbone oriented along the fiber long axis. Therefore, how do we expect increased rigidity to affect conjugated polymer crystallization? While fundamental studies on this topic are lacking, a few works have explored the effect of rigidity on crystallization. Miura et al. 45 studied the effect of rigidity on polymer melt crystallization using molecular dynamics simulations. Figure 3a depicts the crystallization process for semirigid chains. They found that more rigid chains have increased crystalline order and also decreased induction time since they could elongate and align parallel to each other at the same time, while more flexible chains had to stretch out first before they can align and associate together. This is shown in Figure 3b where the semirigid chains rapidly undergo ordering into crystalline domains whereas the semiflexible chains achieve a lower degree of order on a longer time scale. Recently, Yokota and Kawakatsu⁴⁶ modified the classical nucleation theory approach of the HL theory to account for chain stiffness by considering the conformation entropy of polymer chains during crystallization of single chains (chain folding) and multiple chains. They found that, for single chain crystallization, increasing stiffness increased the activation

barrier to form a critical nucleus and lengthened the induction time due to the conformational entropy loss. Additionally, they found that it is easier to form critical nuclei for multiple chains than for single chains as the stiff chains could associate together without having to undergo as much chain folding. These works indicate that rigidity can enhance nucleation and inhibit chain folding to promote intermolecular interactions. Such conclusions are so far in qualitative agreement with the observed behavior of D–A conjugated polymers.

Now we turn our attention to how side chains impact crystallization behavior of conjugated polymers. While there are many different types of side chains used for conjugated polymers such as alkyl, electron donating, electron accepting, and conjugated side chains, to name a few, linear and branched alkyl side chains are the most commonly used for conjugated polymers.⁴⁷ Traditionally, side chains were added to reduce aggregation of conjugated polymers and enhance solubility. Steric effects from side chains reduced intrachain interactions by introducing torsional disorder along the backbone, furthermore resulting in reduced interchain interactions. However, side chain engineering has progressed to serve more varied functions achieved through more complicated effects. Seemingly minute modifications, such as small changes to the side chain length or position, can have significant effects on the final morphology and performance, 48,49 although here we will focus our discussion primarily on how side chains can influence the crystallization behavior of conjugated polymers in general. Panzer and Köhler et al. 50 studied the aggregation and crystallization process of several conjugated polymers in solution mainly through temperature-dependent spectroscopy.

They determined that all of their polymers exhibited the same crystallization behavior upon cooling—disordered coils expand due to backbone planarization and collapse into an aggregated state through an order-disorder phase transition, followed by backbone planarization in the aggregated state, and finally side chain crystallization. Analysis of deconvoluted spectra along with structure determination showed that side chain crystallization occurs as a separate step after backbone crystallization indicating that the conjugated polymer backbone can reach an ordered state while the side chains are still disordered. Other works, however, have shown that alkyl side chains can have more complex effects on crystallization for various conjugated polymers, particularly during film formation. For example, Kline and DeLongchamp et al.⁵¹ found that side chain interdigitation of polythiophenes in film was in fact a preceding requirement to achieve three-dimensional order which would otherwise be unobtainable without interdigitation. Furthermore, the case of competition between the concurrent side chain and backbone crystallization during film casting was studied by Carpenter, Ade et al.⁵² For several D-A conjugated polymers as well as P3HT, they found that side chains can crystallize into layers with unusually high coherence length (>70 nm) at the expense of forming a torsionally disordered backbone layer (Figure 3c). On the other hand, melting of the ordered side chains into a disordered layer results in ordered backbone crystallization (Figure 3d). This competition prevents the side chains and backbones from being highly ordered simultaneously in cast films. The authors were able to take advantage of this behavior by performing slow drop casting to achieve side chain ordering followed by annealing to melt the side chains and produce efficient $\pi - \pi$ stacking resulting in electronic performance exceeding spin-cast films. For further discussion on side chain engineering the reader is directed to several review papers. 47,53

2.2. Flow-Induced Crystallization. As shown above, tuning molecular structure can be an effective means of controlling polymer crystallization. The use of external fields is another means of controlling crystallization. Flow-induced crystallization is one of the most well-studied due to the presence of flows in the industrial processing of polymers. Here we will discuss in general the phenomena of flow-induced polymer crystallization, which has been developed using flexible polymer systems. Studies on flow-induced crystallization of conjugated polymers currently remain scarce despite its potentially large impact in solution processing. The study of flow-induced crystallization started as early as the 1960s when most notably Pennings⁵⁴ observed the formation of fibrillar polyethylene structures upon stirring of a polyethylene solution. This structure was termed "shish kebab" due to the fibrillar core consisting of extended polymer chains and lamellar platelets that nucleate radially along the core. Further work has looked closely on the effect of specific flow fields. Under the influence of sufficiently strong extensional flow it is known that flexible polymers can undergo a coil-to-stretch transition causing the chains to extend and align with the flow direction. 55 The critical condition for this transition to occur is when the extensional strain rate $\dot{\varepsilon}$ applied to the polymer by the fluid overcomes the polymer's relaxation time scale τ . This can be described by the dimensionless Weissenberg number $Wi = \dot{\varepsilon}\tau$ which compares both time scales with the coil-tostretch transition occurring at a critical Wi = 1/2. Additionally, shear flow can also be used to stretch and align polymer chains, although it is typically less effective than extension.⁵⁶ In this

case, a Weissenberg number can also be defined, in which the shear rate replaces the extensional strain rate and the flow effects set in gradually when Wi > 1. For dilute solutions where polymer chains are isolated, shear flow will cause the chains to tumble while they periodically extend and contract. Therefore, shear flow is most useful in concentrated solutions or melts where chains are entangled. As a result of flow-induced chain extension and alignment, flow fields are able to effectively reduce the nucleation barrier and enhance nucleation and growth of flexible polymers to form fibrillar structures consisting of extended parallel chains. In contrast, chain folded lamellae form under quiescent conditions as the time scale to achieve extended parallel chains during crystallization is far longer than for chain folding. Understanding the effect of flow on conjugated polymers is

crucial as flow is inherent to the solution processing methods used to produce conjugated polymer films. This is primarily important for meniscus-guided coating and printing methods, such as blade coating, slot die coating, and bar coating, which are applicable for large-scale, continuous manufacturing. Fundamental studies on the flow effect on conjugated polymers are lacking, although there are some general aspects we can consider. First, conjugated polymers are usually semiflexible, being more rigid compared to typical flexible polymers but still having some degree of flexibility unlike a rigid rod (discussed in Section 2.1). To estimate how the semiflexibility of conjugated polymers influences flow effects such as stretching and alignment we can look at how flexibility influences the relaxation time. For flexible polymers, the relaxation time scale will be the longest relaxation time corresponding to the polymer's conformational relaxation while for rigid rods the relaxation time scale will be inverse to the rotational diffusion coefficient $\tau = (6D_r)^{-1}$ (corresponding to the rod's rotational relaxation) with the dimensionless group now typically referred to as the Peclet number Pe rather than Wi. Hagerman and Zimm⁵⁹ computed the rotational diffusion coefficient of wormlike chains with length to persistence length ratios L/l_p ranging from 0.1 (rod-like) to 5 (wormlike). At very low L/l_p the diffusion coefficient approaches that of a rod; with increasing L/l_n values the diffusion coefficient becomes higher than that of a rod with corresponding length. This indicates that increasing rigidity makes the relaxation process slower, therefore making it easier to achieve flow-induced conformational changes and/or alignment. From another perspective, increased rigidity causes conjugated polymers to adopt a conformation that is more elongated and larger compared to a flexible polymer of similar contour length. The relaxation time is expected to scale with molecular weight or contour length according to $\tau \propto L^{\alpha}$ where the exponent α is 1.5 for flexible polymers⁵⁵ and 3 for rigid rods.⁵⁹ Therefore, we can expect the increased size of conjugated polymers to slow the relaxation time and enhance flow effects. While a fundamental understanding of the effect of flow-induced crystallization and alignment of conjugated polymers is lacking, there is an abundance of phenomenological work looking at the influence of the printing speed, sometimes referred to as the shearing speed, on the final film morphology. Typically what is observed is that at an ideal printing speed fiber growth is enhanced and a large degree of alignment is achieved.^{60,61} In addition, several works have taken it a step further by specifically utilizing fluid flow during solution processing to enhance film morphology and electronic performance of conjugated polymer thin films. For further

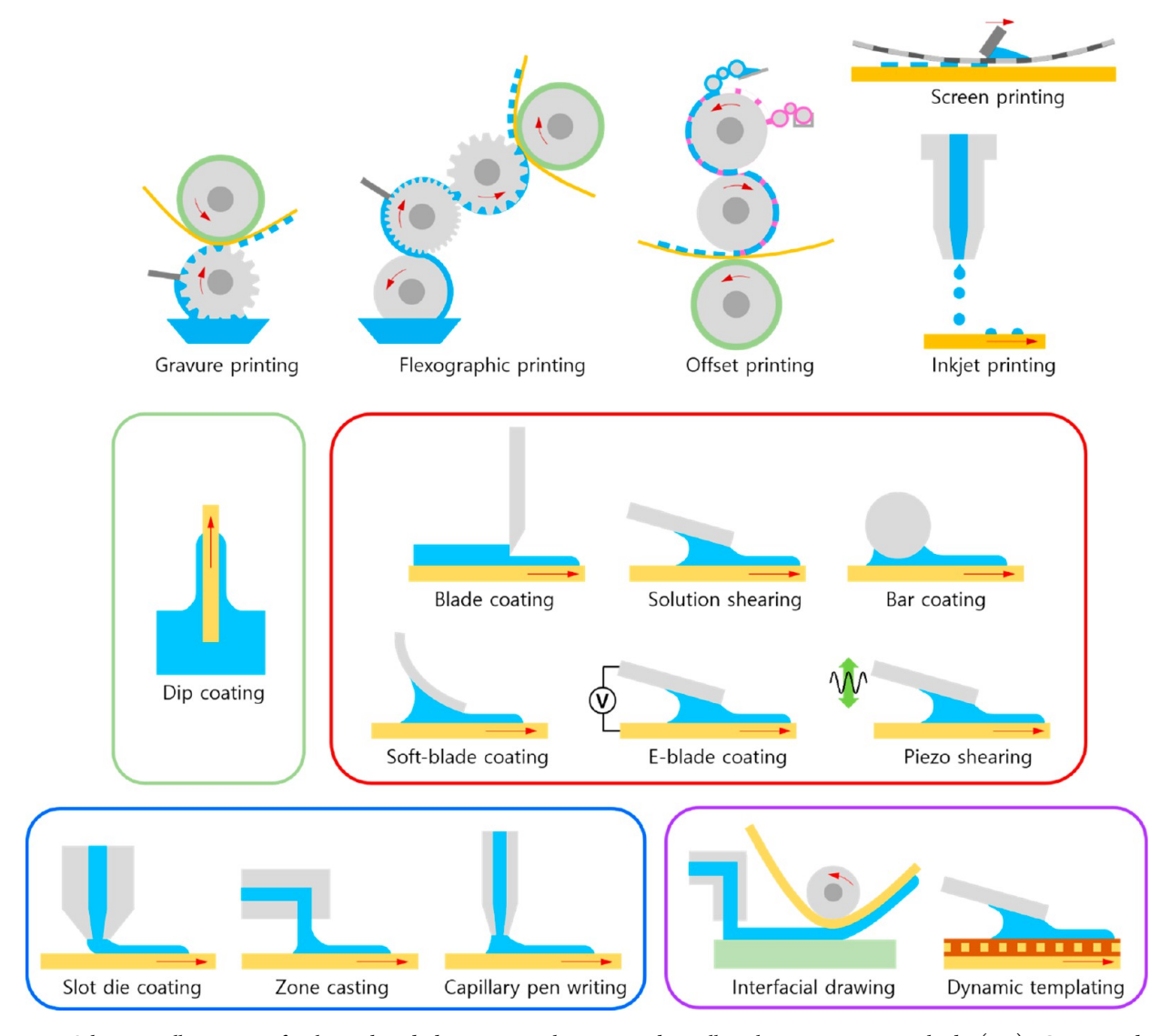


Figure 4. Schematic illustration of solution-based deposition techniques. Industrially relevant printing methods (top). Categorized MGP techniques for printed electronics discussed in this perspective—dip coating (in green box); blade coating and its variations (in red box); slot die coating and its variations (in blue box); and liquid-interface-assisted printing (in purple box). Reproduced with permission partially adapted from refs 66 and 88. Copyright 2014, 2017 The Royal Society of Chemistry.

discussion on flow-induced crystallization of organic electronics we direct the reader to our previous reviews. 62,63

3. COATING AND PRINTING TECHNIQUES AND FUNDAMENTALS

3.1. Coating and Printing Techniques. Common solution-based coating and printing techniques, e.g., gravure printing, offset printing, flexographic printing, and screen printing, have been broadly employed in industrial processes such as product/food packaging, print media, and clothing. For organic electronics which are emerging in markets related to flexible displays, solar cells, and sensors, commonly pursued coating and printing methods include slot die coating, blade coating, and inkjet printing, which are often implemented in a roll-to-roll manner for high throughput and low cost. ^{64,65} A key challenge in the area of printed organic electronics lies in the precise control of film morphology during solution deposition. Among a wide range of solution-processing methods for organic semiconductor deposition, meniscus-guided printing (MGP) techniques have been extensively pursued for

morphology control owing to the inherent directionality of the process and the ability to control solvent evaporation. MGP techniques generally involve an ink applicator and a substrate which sandwich the ink solution and thus establish a meniscus. The ink applicator is translated linearly parallel to the substrate during MGP and guides the motion of the meniscus through a capillary force. Here, we provide a brief summary of MGP techniques used in recent years such as dip coating; blade coating and its variations including solution shearing, bar coating, soft-blade coating, electrical (E)-blade coating, and piezo shearing; slot-die coating and its variation including zone casting and capillary pen writing; and interfacial related printing such as interfacial drawing and dynamic templating (Figure 4). A comparison of the features of various printing and coating methods is given in Table 1. 64,66,67

Dip coating is the simplest MGP technique in which a substrate is vertically drawn out from a solution reservoir. Key parameters such as withdrawal velocity and substrate/solution temperature influence the development of concentration gradients and fluid flow within the meniscus. Solvent choice

Table 1. Summary of Printing Parameters of Printing and Coating Techniques Discussed

Technique	$\begin{array}{c} Speed \\ (m \ min^{-1}) \end{array}$	Ink viscosity (cP)	Resolution (μm)
Gravure printing	1 - 1000	<10-1000	<10
Offset printing	1000	100-100 000	10
Flexographic printing	1-1000	<10-1000	10-50
Screen printing	50-150	100-100 000	10->50
Inkjet printing	1-500	<11-100	10-50
Dip coating	<1-10	50-500	_
Blade coating and its variations	1-100	0.1-10	_
Slot die coating and its variation	1-1000	10-100 000	10-50
Zone casting	0.003-10	_	_
Interfacial drawing	0.1 - 1	1-10	_
Dynamic templating	0.03-6	0.1-10	_

is particularly important because of its effect on the rate of solvent evaporation and surface wettability. Kim and Park et al. 68 recently demonstrated the effect of solvent vapor on film uniformity of dip-coated P3HT. Because the drying film is constantly exposed to the solvent vapors from the reservoir, the film morphology worsens and crystallinity decreases during the withdrawal process. The authors demonstrated that an additional solvent vapor annealing step on the dip-coated film in the coating chamber improved film uniformity and crystallinity. Dip coating has also been utilized to produce a monolayer-thick film of conjugated polymer by optimizing the coating speed and preaggregation state. 69 Blade coating has been widely adopted for aligning conjugated polymers in thin films. In blade coating, a sharp blade held perpendicular or angled to the substrate transports a solution droplet across the substrate. A forward meniscus is formed at the trailing edge, and the ink reservoir upstream of the meniscus is exposed to the ambient. During coating, polymer chains are subject to evaporation- and substrate-driven flow which we detail in the next section. Several variations of the blade coating technique have been used for polymer chain alignment in printed films, including bar coating, solution shearing, brush painting, soft blade coating, electrical blading, piezo shearing, etc. In bar coating, a cylindrical or rectangular bar is used instead of a blade. Bucella, Facchetti, and Caironi et al. 70 used a wired barcoating technique that yielded highly aligned naphthalene diimide-bithiophene-based copolymer P(NDI2OD-T2) films as thin as a submonolayer. Alignment was attributed to using fibril-like preaggregated solutions as the ink for bar coating. Another variation of blade coating is solution shearing where the blade is held almost parallel to the substrate, instead of at a high angle or perpendicular to the substrate. Shaw, Bao et al. 60,71 reported that solution shearing can induce uniaxial alignment in both the crystalline and amorphous regions of DPP2T-TT polymer thin films. Besides using flat, planar blades, lithographically patterned microstructured shearing blades have been developed to induce extensional flow and to enhance the shear rate. 72-74 Soft blades such as a flexible, solution resistant perfluoropolyether or natural hair brush have also been used to uniaxially align and control aggregation of conjugated polymers for enhanced charge transport. 61,75 Recently, an external electric field was applied to the coating blade during solution shearing that led to 2-fold enhancement in DPP polymer chain alignment attributed to the dielectrophoresis effect. Teixeira da Rocha and Mannsfeld et al. 77 developed a piezo-shearing technique where a piezo crystal was mounted on top of a coating blade to produce high-frequency vibrations. This method was able to alleviate the "stick-andslip" phenomenon commonly encountered due to meniscus instability, thereby resulting in ultrathin, uniform polymer films. Slot die coating is a prominent MGP method for industrial applications being extremely high throughput and tolerant to high ink viscosity. Slot die coating involves a hollow die head through which an ink solution is dispensed onto a moving substrate. The capability of slot die coating was demonstrated by fabrication of highly efficient polymer solar cells and organic light emitting diodes. 78,79 The zone casting technique is similar to slot die coating, in which solution is continuously fed to a solution droplet as it is dragged beneath the nozzle.80 Capillary pen writing, also known as "hollow-pen writing", was demonstrated to deposit and pattern conjugated polymers on a desired substrate. 81 Recent advances on penbased writing electronics and applications can be found more in a relevant review.⁸² Very recently, interfacial drawing was reported to print polymer films on a floating liquid interface which can be transferred to the substrate using a roll-to-roll process.⁸³ This method enables producing multilayered architectures and uniform printing on nonplanar, rough, or porous substrates as the films are solidified prior to the deposition. Our group recently developed a dynamic-templatedirected solution coating approach where an ionic or hydrogen-bonded liquid hosted in nanoporous media or in a polymer matrix serves as the coating substrate in MGP.84-87 Distinct from the interfacial drawing approach, the dynamic template can direct polymer assembly by maximizing favorable interactions with conjugated polymers at the interface through cooperative multivalent interactions, leading to highly aligned, highly crystalline polymer thin films. These studies will be discussed in detail in Section 4.2.

3.2. Coating and Printing Fundamentals. 3.2.1. Printing Fundamentals. In MGP, a volatile conjugated polymer solution is guided over a substrate by an ink applicator or print head. As the solvent evaporates a conjugated polymer film is deposited onto the substrate to be used as the active layer of the electronic devices. To understand solution printing we will discuss here the physical processes that occur in various printing regimes and the effect of different printing parameters. Ultimately, the printing behavior is determined by the competition between solvent evaporation and viscous forces imparted by the moving head or substrate (i.e., printing speed), although other factors can further influence the polymer crystallization process in specific cases. Self-metered MGP techniques such as blade coating and its variations discussed previously are well generalized by the physical processes described here which are able to capture the main features of solution printing seen in practice. Even for other MGP techniques, which have more distinct variations, the fundamental physical processes described are largely transferrable, and a similar analysis can be applied with changes to certain assumptions or new assumptions. For example, in the cases of dip coating and slot die coating, additional driving forces for flow are present in the form of gravity and pressure, respectively. In other cases such as piezo shearing or dynamic templating, different boundary conditions could be applied to capture the unique features of these techniques. The key physical processes are briefly described here. For further discussion one can find more information in our previous review.63

To understand the different regimes, let us first examine the printing process when printing speeds are low. At slow printing speeds in MGP, the printing regime is termed the evaporation regime as the evaporation rate (when expressed as an evaporation velocity) is significantly faster than the printing speed. In this regime, the flow in the meniscus and deposition of the film is similar to that of an evaporating droplet with solute. This was largely explained by Deegan et al. 89 where the formation of ring stains around drying droplets was termed the coffee ring effect. As the evaporative flux is largest near the contact line, fluid must flow outward toward the contact line to maintain the mass balance. As a result, solute in the droplet is carried by the flow to the contact line, forming a ring. These findings were further explored and confirmed by Hu and Larson who carried out experiments along with a lubrication theory analysis and computational finite element method (FEM) analysis in order to solve for the evaporative flux and flow field. Another phenomenon to note here is the possibility of Marangoni flow in the meniscus which can occur due to surface tension gradients caused by gradients in temperature or solute concentration. Hu and Larson⁹¹ also carried out a study on Marangoni flow in evaporating droplets revealing that Marangoni stresses can change the flow field significantly and produce recirculation. At the other extreme, when printing speeds are very fast, solvent evaporation is negligible and viscous forces imparted by the moving printhead or substrate dominate the printing process. This regime is commonly referred to as the Landau-Levich (LL) regime as it resembles the original dip coating problem where flow is produced from the withdrawal of a plate from a liquid bath.⁹² In this regime, evaporation is negligible and a liquid film is dragged out across the substrate which then evaporates at time scales much longer than that of printing. In this regime, the printing process more closely resembles the coating of a nonvolatile liquid film over a surface.

Several works have studied in detail how film deposition changes as the printing speed is continuously varied from slow to fast across regimes. ^{60,92–94} Le Berre et al. ⁹² investigated this during blade coating of phospholipid films at various speeds. They found film thickness to scale with printing speed to the powers –1.1 and 0.76 for the evaporation regime and LL regime, respectively, with a transition in between. At low speeds, in the evaporation regime, evaporation dominates the printing process, and evaporatively induced capillary flows are much faster than flow produced by the moving print head or substrate (Figure 5a). It can be assumed that film deposition occurs at the contact line in this regime and so a mass balance analysis can be used which yields the following dependence of film thickness on printing parameters, ⁹²

$$h_{evap} = \frac{C}{\rho} \frac{Q_{evap}}{L} v^{-1} \tag{1}$$

where C is the bulk solute concentration, ρ is the solution density, Q_{evap} is the evaporation rate of solvent, L is the width of printed film, and ν is the printing speed. The analysis indicates an inverse relation between the film thickness and the printing speed, in close agreement with the experimental film thickness scaling with printing speed to the power -1.1 (Figure 5c). This can be understood by recognizing the following physical underpinning: evaporation rate is constant regardless of printing speed in this regime, and thus the same amount of material should be deposited regardless of speed; in

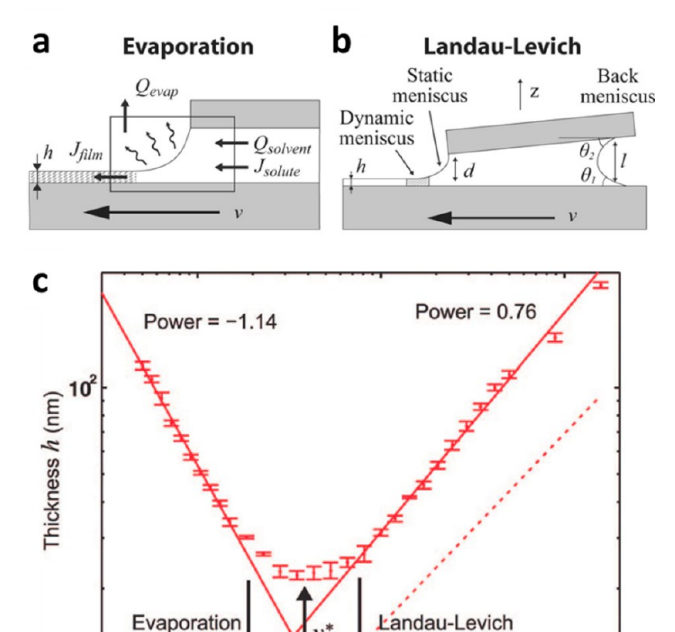


Figure 5. Evaporation and Landau—Levich regimes during MGP. (a) Schematic of mass balance over the meniscus in the evaporation regime. (b) Schematic of the meniscus in the LL regime with geometric parameters. (c) Experimentally measured thickness of phospholipid films produced by MGP. Reproduced with permission from ref 92. Copyright 2009 American Chemical Society.

10³

Speed v (µm/s)

10⁴

10²

other words, if a film is printed faster it must be thinner to maintain its mass flow rate out of the system. As speed increases further into the LL regime, this dependence changes as more liquid is supplied than can be evaporated and so film thickness starts to increase. Le Berre and colleagues carried out a similar analysis to the original Landau—Levich problem for this regime (Figure 5b) finding the expression for film thickness to be

$$h_{LL} = 1.34 \frac{C}{\rho} \frac{l}{\cos \theta_1 + \cos \theta_2 - \frac{l^2}{2\kappa^{-2}}} Ca^{2/3}$$
 (2)

where κ^{-1} is the capillary length, $Ca = \mu v/\gamma$ is the capillary number (with μ and γ being the solution viscosity and surface tension, respectively), and θ_1 , θ_2 , and l are the back meniscus contact angles and gap height as shown in Figure 5b. The result finds a theoretical dependence of film thickness on speed to be to the power of 2/3, which is also close to their experimental value of 0.76 (Figure 5c). In this regime, viscous forces imposed by the substrate drag out a liquid film much faster than it can be evaporated. As a result, the liquid film coating the substrate immediately retains the initial bulk concentration and then proceeds to undergo static drying. Film thickness increases in this regime since at a higher speed a thicker liquid film is dragged out and so a thicker film is left after slow drying.

To further understand the physical processes that occur in these regimes, Doumenc and Guerrier⁹³ performed FEM simulations of MGP using lubrication theory to model the meniscus. Our group also carried out similar simulations alongside experimental MGP of conjugated polymers while

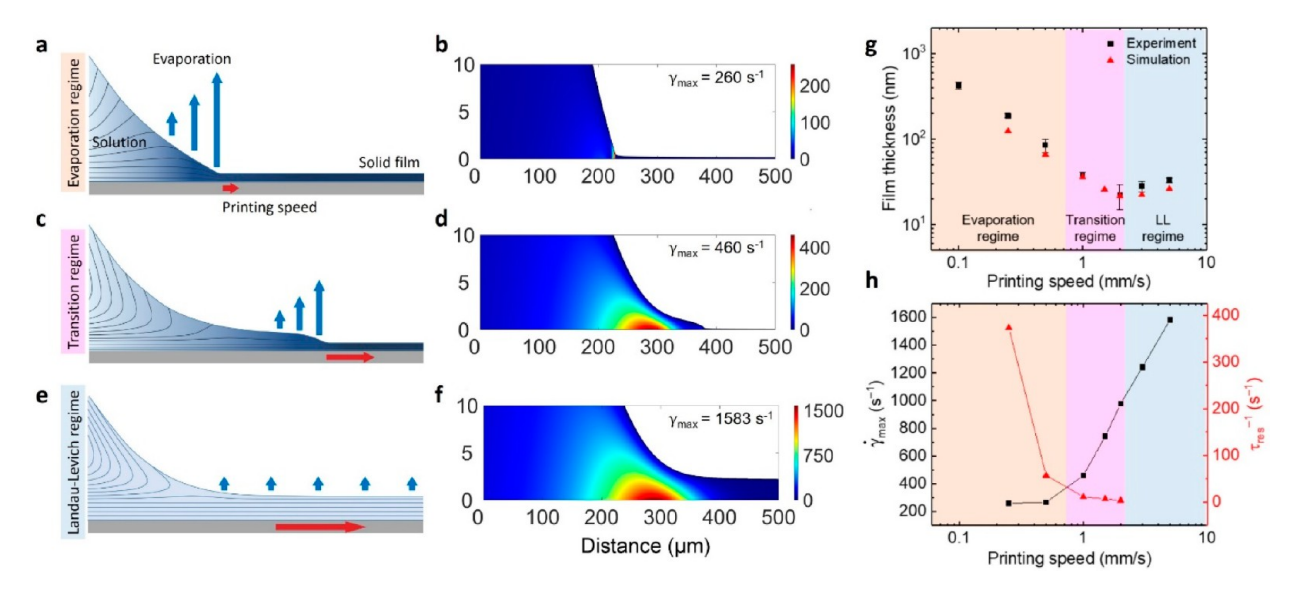


Figure 6. Meniscus guided printing regimes resulting from the competition between evaporation and viscous forces imparted by the moving substrate (printing speed). (a—f) Schematic representation of the meniscus in the evaporation, transition, and LL regimes, respectively (left), and simulated shear rates in the meniscus for the three printing regimes with increasing shear as the printing speed increases (right). (g) Comparison between experimentally measured and simulated film thicknesses as a function of printing speed. (h) Peak strain rate and inverse residence time as a function of printing speed. From ref 94. Copyright Park, K.S. and Kwok, J.J., et al., some rights reserved; exclusive licensee American Association for the Advancement of Science. Distributed under a CC BY-NC 4.0 License (http://creativecommons.org/licenses/by-nc/4.0/).

expanding the simulation with a focus on the meniscus flow field.⁹⁴ To adequately describe the MGP process three main physical phenomena were considered: solvent vapor diffusion in the gas phase governed by Fick's law, incompressible fluid flow within the meniscus governed by the Navier-Stokes equation, and transport of the nonvolatile solute within the meniscus governed by convection-diffusion. The coupling of these physics with appropriate boundary conditions enables modeling of the convective assembly process over a wide range of printing parameters, especially the printing speed. There are several key assumptions and boundary conditions used to model the system. First, lubrication approximation is used. Next, flow in the meniscus is driven by capillarity so that the pressure gradient is the gradient of meniscus curvature $\partial P/\partial x$ = $\partial^3 h/\partial x^3$ where h is the meniscus height profile along the printing direction (x-direction) and the velocity of the fluid at the substrate boundary is the printing speed v_{sub} (no-slip). In the gas phase, the solvent vapor concentration is determined by the vapor pressure $P_{vap}(T)$ of the solvent at the temperature T at the meniscus free surface and goes to zero a sufficient distance away from the meniscus. The vapor pressure can be determined with either the Antoine equation or the Clausius-Clapeyron equation (evaporative cooling and Marangoni effects are neglected for simplicity). Finally, there is transport across the free surface boundary between the meniscus and the gaseous domains due to evaporation. This last condition is critical in order to couple the fluid flow with vapor diffusion and properly equilibrate the meniscus shape. This is accounted for by applying the kinematic boundary condition with evaporative flux at the free surface:

$$\vec{v_I} \cdot \vec{n} = (\vec{u} - \vec{v}_{evap}) \cdot \vec{n} \tag{3}$$

where

$$\vec{v}_{evap} = \frac{\vec{J}_{evap}}{\rho} = -\frac{D_g}{\rho} \frac{\partial c}{\partial y} \bigg|_{y=0}$$
(4)

and $\overrightarrow{v_I}$ is the velocity of the interface, \overrightarrow{n} is the unit normal of the interface, \overrightarrow{u} is the velocity of the fluid at the interface, $\overrightarrow{v}_{evap}$ is the evaporation velocity, $\overrightarrow{J}_{evap}$ is the evaporative flux, D_g is the diffusion coefficient of the solvent vapor, and c is the solvent vapor concentration field in the gas phase with y being in the direction of the substrate normal. The governing equations for the main physical processes are then

$$\frac{\partial c}{\partial t} = D_g \left(\frac{\partial^2 c}{\partial x^2} + \frac{\partial^2 c}{\partial y^2} \right) \tag{5}$$

$$\frac{\partial Q}{\partial x} + \frac{\partial h}{\partial t} = -v_{evap} \tag{6}$$

$$\frac{\partial(\phi Q)}{\partial x} + \frac{\partial(\phi h)}{\partial t} = \frac{\partial}{\partial x} \left(h D \frac{\partial \phi}{\partial x} \right) \tag{7}$$

where t is the time, Q is the 2D volumetric flux in the x-direction, ϕ is the solute concentration in the meniscus, and D is the diffusion coefficient of the solute in the solvent. These governing equations describe the solvent vapor diffusion, total mass balance in the meniscus, and solute mass balance in the meniscus, respectively. Doumenc and Guerrier found the simulated dried film thickness' dependence on printing speed to agree with theory, having exponents near -1 and 2/3 for the evaporation and LL regime, respectively. By carrying out these simulations they were also able to understand how concentration and viscosity impacted the regimes which will be discussed in the following section on printing parameters. By the same method, we were able to simulate MGP of conjugated polymers and found good agreement between the predicted film thickness and the experimentally measured

thickness of the conjugated polymer films, indicating sufficient modeling of the MGP process. Furthermore, our group additionally investigated the flow field within the meniscus. We determined the flow field $\vec{u} = (u_x, u_y)$ to be described by

$$u_x = -\frac{\gamma}{\mu} \frac{\partial^3 h}{\partial x^3} \left(\frac{y^2}{2} - hy \right) + v_{sub}$$
 (8)

$$u_{y} = \frac{\gamma}{\mu} \left[\frac{\partial^{4} h}{\partial x^{4}} \left(\frac{y^{3}}{6} - \frac{hy^{2}}{2} \right) - \frac{\partial^{3} h}{\partial x^{3}} \frac{\partial h}{\partial x} \frac{y^{2}}{2} \right]$$
(9)

allowing the flow field to be calculated after the meniscus height profile was determined. With the flow field the strain rate tensor and strain rate can be calculated as $E = (\nabla \vec{u} + \nabla \vec{u})$ T)/2 and $\dot{\gamma} = \sqrt{2E:E}$, respectively. Our group carried out a combined experimental and simulation study to understand the evolution of the meniscus as a function of the printing speed with a particular focus on the flow field and fluid strain rates. At low printing speeds, we observed the evaporation regime where capillary-induced flows are dominant over the printing speed (Figure 6a) and so shear rates within the meniscus are weak as seen in Figure 6b. Here, the meniscus adopts a constant curvature from the bulk region to the contact line. At intermediate speeds, the evaporation rate and the viscous forces imparted by the substrate are both important, and a liquid film is partially dragged out (Figure 6c) resulting in a region of higher shear rate to form in the meniscus (Figure 6d). This transition regime is marked by the change in meniscus shape where the emerging presence of the partially dragged out meniscus causes meniscus curvature to no longer be constant near the contact line. At higher speeds in the Landau-Levich regime the liquid is dragged out much faster than it can evaporate resulting in a thicker bulk liquid film being dragged out with the shear rate increasing further (Figure 6e,f). The simulated film thicknesses were found to agree well with the experimentally measured conjugated polymer film thicknesses over a wide range of printing speeds (Figure 6g), and the three regimes can be further identified by their film thickness dependence. To understand how the meniscus printing flows can influence the morphology, the max meniscus strain rate was plotted along with the inverse residence time (from its position to the contact line) as a function of printing speed (Figure 6h). In the evaporation regime the shear rate was very low, thereby preventing any flow-induced alignment or conformational change from occurring. In the LL regime, since a bulk liquid film is dragged out the residence time of the polymer increases drastically, allowing the strained polymer chains to relax before solidification. The intermediate speeds were termed the "transition regime" as it is at this transition between the evaporation and LL regimes that the shear rates begin to increase while residence times remain low allowing for an optimal condition for enhancing conjugated polymer planarization and alignment.

3.2.2. Printing Parameters. It is useful to understand how different printing conditions can affect the MGP process and subsequent film characteristics. Here we will discuss how various tunable parameters influence printing regimes and/or conjugated polymer assembly. The effect of printing speed was discussed in the previous section and is the main way to modulate the printing regime by tuning the degree of viscous forces imparted by the printhead or substrate. Tuning the evaporation rate is another way to achieve this. The key

parameter in this case is the solvent vapor pressure which affects the evaporative flux at the free surface. The solvent vapor pressure can be adjusted by changing the solvent or the temperature, both of which have the secondary effects discussed below. Alternatively, the evaporation rate can be adjusted by enhancing the convection of the solvent vapor above the meniscus by flowing nitrogen or by adjusting the ambient pressure using a vacuum (aspiration), which can also induce convection. By increasing solvent vapor pressure, the evaporative flux is enhanced due to a larger concentration gradient between the free surface and the surroundings. As a result, film thickness increases in the evaporation regime and the transition regime shifts to higher speeds as evaporation becomes stronger, and faster printing speeds are required to begin dragging out a liquid film. To highlight the prominent dependence on the solvent vapor pressure of the MGP regimes, work by Janneck et al. demonstrated that an estimate of the optimal printing speed of organic small molecules could be predicted solely based on the evaporation of the solvent. 95 For a wide variety of organic solvents ranging from high (dichloromethane, bp 39.6 °C) to low vapor pressure (tetralin, bp 208 °C), the printing speed that yielded optimal film morphology occurred at the equilibrium front evaporation speed (i.e., the speed a static meniscus recedes due to evaporation) which depends on the solvent vapor pressure as determined by the enthalpy of vaporization and printing temperature. The result here is quite interesting as it is qualitatively similar to the optimal transition regime proposed by our group⁹⁴ where the printing speed is of similar order to the evaporation velocity.

The solvent effect goes beyond the effect of vapor pressure on evaporation rate. The effect of solvent quality is very well studied and has been used to tune the polymer conformation or the degree of aggregation in solution and in some cases can give rise to or inhibit the formation of liquid crystalline (LC) mesophases. This can change the polymer solution state and affect subsequent film morphology as will be discussed in Section 4.3. Given that the solvent effect convolutes both the solvent quality effect and the solvent vapor pressure effect, it is important that when studying the solvent quality dependence of printed film morphology, either the vapor pressure be matched by optimizing the printing temperature or the films are compared at the same regime and film thickness rather than printing speed. Doing so ensures that differences in the film morphology are due to the solvent quality rather than changes in the printing regime due to the vapor pressure differences. Likewise, the printing temperature brings convoluted effects too. While one of the main consequences of tuning printing temperature is changing the solvent evaporation rate and therefore the printing regime, tuning temperature can also drastically change the conjugated polymer solution state. This has been explored in detail by Panzer and Köhler et al.50 where they demonstrate that reducing temperature forms aggregates through an order-disorder transition where random coils first expand and then collapse into disordered aggregates which then proceed to planarize and

Another factor that can influence the film deposition process is the initial solution concentration. Doumenc and Guerrier looked at the effect of the solution concentration on the printing regimes using simulation. They found that film thickness increased over all printing speeds but more so in the LL regime resulting in the transition regime shifting to lower

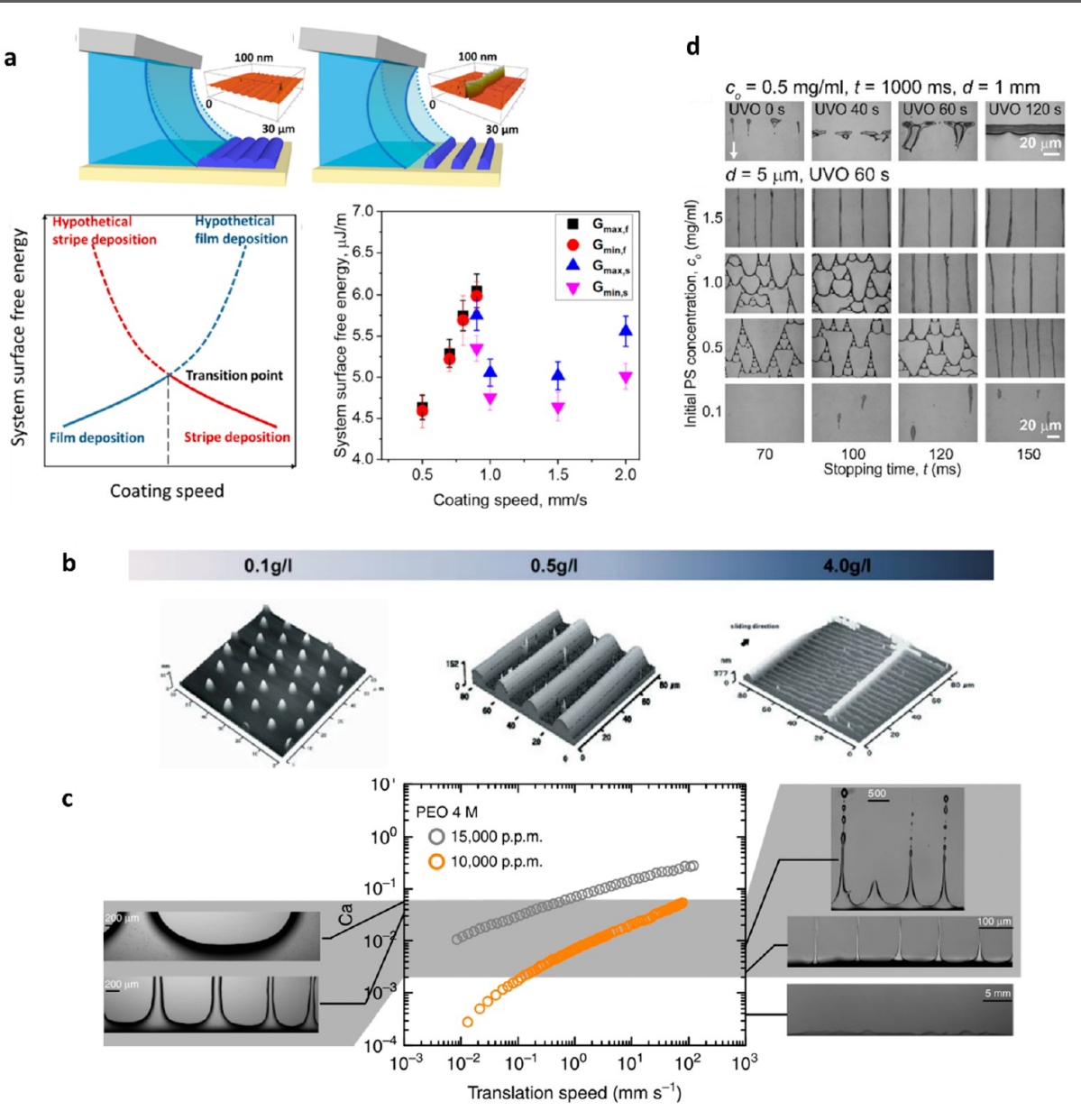


Figure 7. Examples of instabilities formed during solution coating. (a) Stick-and-slip instability from surface free energy. Reproduced with permission from ref 96. Copyright 2018 American Chemical Society. (b) Morphology transitions occurring in concentration regimes. Reproduced with permission from ref 97. Copyright 2005 Wiley-VCH Verlag GmbH & Co. KGaA, Weinheim. (c) Filament pattern formation dependent on capillary number. Reproduced from ref 98. "Taming contact line instability for pattern formation" by Deblais, A., et al. is licensed under CC BY 4.0. To view a copy of this license, visit http://creativecommons.org/licenses/by/4.0/. (d) Hyperbranched structures formed by Marangoni instability. Reproduced with permission from ref 99. Copyright 2015 Wiley Periodicals, Inc.

speeds. Naturally, as concentration increases, the film thickness increases in the evaporation regime simply due to the presence of more material. In the LL regime, the film thickness also increases due to higher concentrations, but since the viscosity of the solution increases as well the viscous forces are also enhanced and therefore a thicker liquid film can be dragged out. As a result, film thickness scales with bulk concentration in the evaporation regime but increases even more so in the LL regime due to viscosity increase. This can also be seen when they simulated an increase in molecular weight at the same concentration and found only the LL regime film thicknesses to increase.

One last important parameter to consider is the substrate material. The substrate can have a variety of different effects on printing. Here we will discuss the effect of substrate on the meniscus properties and how this effects printing in general. Besides influencing meniscus properties, substrates can drastically influence the crystallization processes of conjugated polymers by tuning polymer—substrate interactions or surface roughness or by other means as will be discussed in Section 4.2. The most obvious effect the substrate has is by altering the dynamic receding contact angle of the meniscus depending on the surface energies of the system. When contact angles are decreased the evaporative flux becomes enhanced near the contact line. As mentioned before, the result is that the films become thicker in the evaporation regime and the transition regime shifts to higher speeds as stronger viscous forces are required to drag out a liquid film.

While ideally meniscus guided printing is a steady state process, instabilities can arise during printing due to various

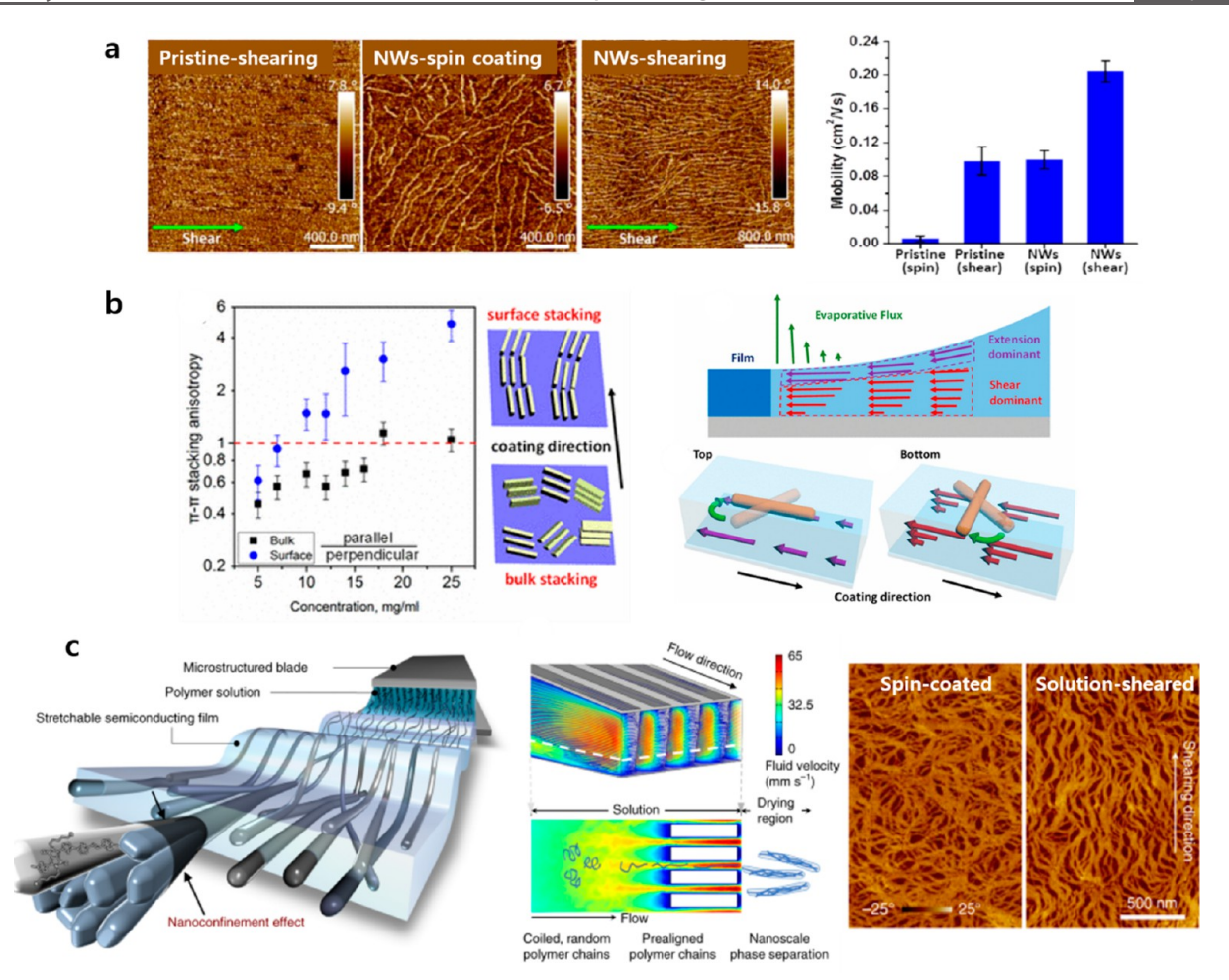


Figure 8. Flow-directed assembly by engineering flow. (a) AFM images of P3HT films sheared at 2.0 mm/s using a pristine solution, spin-coated, and sheared at 2.0 mm/s using a preaggregated solution (left). Charge carrier mobility comparison of the P3HT films prepared by the corresponding system (right). Reproduced with permission from ref 102. Copyright 2016 American Chemical Society. (b) Solution concentration dependent in-plane alignment obtained from edge-on π - π stacking peak on grazing incidence X-ray diffraction (GIXD) and the corresponding schematic showing different alignments at the film surface vs the bulk (left). Three-dimensional view of the in-plane alignment mechanism for an anisotropic particle in the extensional and shear flow field (right). Reproduced with permission from ref 107. Copyright 2017 American Chemical Society. (c) Solution-shearing method using a blade with line structures to enhance shear stress as well as induce extensional flow (left). Unidirectionally aligned stretchable semiconducting films when compared to their spin-coated counterparts (right). Reproduced with permission from ref 72. Copyright 2019 Springer Nature.

reasons such as substrate surface energies. Our group 96 studied the stick-and-slip instability that occurs during printing of conjugated polymers where the meniscus repeatedly pins and depins resulting in the formation of stripes as the contact line moves (Figure 7a, top). We found that lower speeds produced films while faster speeds produced isolated stripes. A film-tostripe transition occurred at a critical printing speed where both film and stripes can occur. To explain this phenomenon we proposed a model based on the various interfacial free energies as well as the meniscus and polymer deposit geometry. We found that the total system surface free energy increases with speed in the film regime and then decreases into the stripe regime with the energies matching at the critical printing speed (Figure 7a, bottom). Therefore, we hypothesized that the film-to-stripe transition occurs in order to reduce the system surface free energy. Yabu and Shimomura⁹⁷ studied the morphological transitions occurring during blade coating of polystyrene. They found polystyrene to form dots, stripes, and ladder patterns depending on the concentration (Figure 7b). For dilute solutions, stick-and-slip phenomena formed stripes

that dewetted into dots. At high concentrations, the stripes produced by stick-and-slip persisted, forming lines. At even higher concentrations, a ladder pattern is formed consisting of stripes perpendicular to the coating direction as well as thick lines parallel to the coating direction. The authors attributed this to a combination of stick-and-slip instability and fingering instability caused by Marangoni flow and increased viscosity. Deblais and Kellay et al. 98 studied the transition from smooth contact lines to filament formation during the flexible blade coating of polyacrylamide (Figure 7c). They found that pattern formation depends on the capillary number (Ca) with uniform coating at low Ca, unstable rivulets and droplet formation at intermediate Ca, and long slender filaments at high Ca. Liu, Monteux, and Crosby et al. 99 studied the formation of hyperbranched structures during move-and-stop coating of polystyrene due to instabilities. They used in situ microscopy to understand the formation of the hyperbranched structures. When the substrate moves, a finger first forms at the meniscus contact line due to a Marangoni instability and friction. The finger then thins out during the coating process and separates

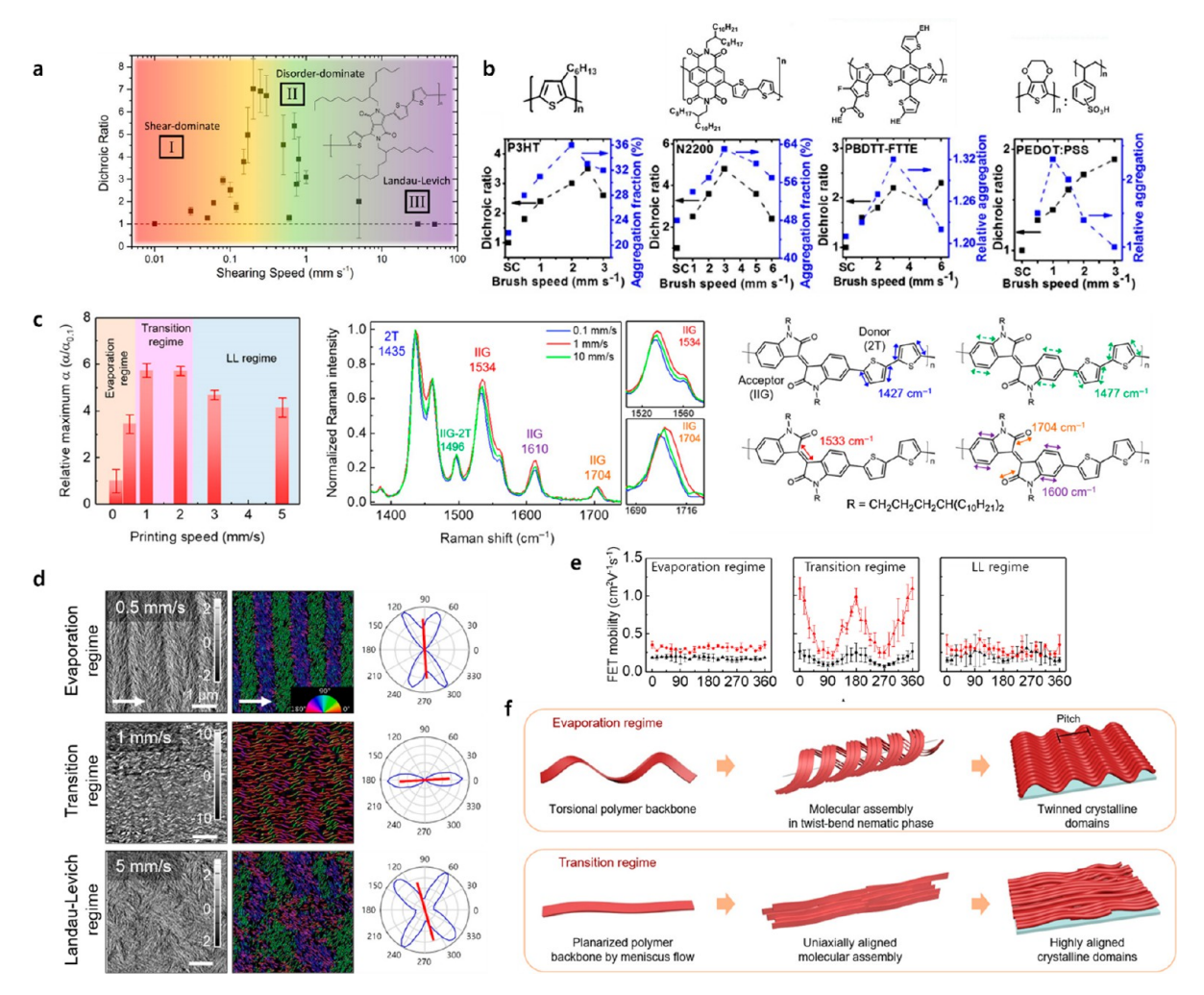


Figure 9. Printing regime directed morphology. (a) Optical dichroic ratio as a function of shear speed for the PDPP3T films. Image reproduced with permission from ref 71. Copyright 2018 American Chemical Society. (b) Molecular structures of the conjugated polymer used in this study (top). Optical dichroic ratio and aggregation fraction (or relative aggregation) of printed polymer films as a function of printing speed and spin-coated counterparts (bottom). Reproduced with permission from ref 61. Copyright 2017 National Academy of Sciences. (c) Relative maximum absorption coefficient ($\alpha/\alpha_{0.1}$) change of PII-2T films in each regime (left). Normalized Raman scattering spectra of PII-2T films printed in each regime (middle). Illustration of representative Raman-active vibrational modes calculated for PII-2T oligomers (right). (d) AFM phase images (left), corresponding orientation mapping analysis (middle), and pole figures of the fibril orientation distribution (right) for the films printed in each regime. (e) Field-effect mobility for films made in each regime as a function of φ. Black and red data points correspond to before and after annealing, respectively. (f) Schematic illustration of the printing-flow-induced PII-2T assembly mechanism. (c-f) reproduced from ref 94. Copyright Park, K.S. and Kwok, J.J., et al., some rights reserved; exclusive licensee American Association for the Advancement of Science. Distributed under a CC BY-NC 4.0 License (http://creativecommons.org/licenses/by-nc/4.0/).

into two branches until the substrate stops. Once the substrate moves again, fingers form at the branches to form the self-similar structure. The formation and geometry of the hyperbranched structure depended on the substrate surface energy and viscosity as well as the moving distance and stopping time (Figure 7d). These works demonstrate that at the right conditions a combination of various parameters can give rise to interesting meniscus dynamics and pattern formation which can potentially be exploited for lithography free patterning.

4. STRATEGIES TO CONTROL MORPHOLOGY DURING SOLUTION COATING/PRINTING

In this part, we present the processing related strategies that include (i) flow-directed assembly, (ii) surface modification, and (iii) tuning assembly pathways. In each section, we discuss valuable insights into the molecular assembly film morphol-

ogy—device performance relationship. We would like to note that this is not a comprehensive review of all important morphology control strategies developed; rather we choose to highlight a few recent strategies that are of direct relevance to processing and/or innovation in solution printing.

4.1. Flow-Directed Assembly. *4.1.1. Engineering Flow.* Fluid flow is ubiquitous across all solution processing techniques and thus designing flows is an integral part of morphological control for high performance organic electronics. For conjugated polymers, extensional and shear flow can expedite nucleation through flow-induced conformation change, facilitating the control of crystallization, microphase separation, and domain alignment. First, simple shear has been employed to promote nucleation and crystallization from originally dispersed polymer solutions. Wie and Mackay et al. ¹⁰⁰ demonstrated that long and crystalline fibrils of P3HT were formed as a result of a continuous shear application to the

concentrated polymer solution. The authors proposed that Brownian motion can bring the molecules together while shear induced the favorable molecular conformation, allowing fibrillike crystallization. Wang and Reichmanis et al. 101 reported a microfluidic system utilizing shear along with cooling and UV treatment that allowed enhanced P3HT solution aggregation and alignment. The P3HT films produced through this flow system resulted in decreased $\pi - \pi$ stacking distance from 3.93 to 3.72 Å and increased hole mobility from an average of 0.013 to 0.16 cm² V⁻¹ s⁻¹ when compared to their spin-coated counterparts made using pristine solutions. Shear also has been used to induce uniaxial alignment of polymer molecules from preaggregated solutions. Chang and Egap et al. 102 demonstrated shear-directed aligned arrays of P3HT nanowires obtained using a preaggregated nanowire solution, exhibiting over 33-fold enhancement in the average carrier mobility compared to randomly oriented spin-coated nanowire films or sheared pristine films (Figure 8a). The effect of shear was much stronger to preaggregated nanowires over single polymer chains because the nanowires are more rigid and often exhibit high aspect ratios with lengths up to a few micrometers in solution. In the past few years, shear flow has been effectively applied to control D-A conjugated polymer alignment and crystallization mediated by a lyotropic LC phase. 75,94,103-106 Our group⁹⁴ recently reported a shear-directed LC-mediated PII-2T assembly mechanism. It was observed that the shear eliminated a lyotropic twist-bend LC phase upon backbone planarization resulting in highly aligned printed polymer thin films. As such, we observed a 4-fold increase in charge carrier mobilities. A more detail discussion regarding LC-mediated shear-induced alignment is included in Section 4.3.2.

Extensional flows have been found to be most effective at extending polymer chains, although shear can induce chain extension in polymer melts and aggregated/concentrated solutions in which polymers are entangled. Wang and Reichmanis et al.⁷⁴ implemented structured coating blades to induce extensional flow with UV irradiation, leading to enhancement of P3HT crystallization and alignment. The wave-like structural blade promoted extensional flow from the change in fluid velocity in compression and expansion regimes. The long, highly aligned P3HT nanowires in the film were achieved using the wave patterned blade, while randomly oriented short nanowires were obtained using the straight patterned blade. The charge carrier mobility of highly aligned films ($\sim 13 \times 10^{-2} \text{ cm}^2 \text{ V}^{-1} \text{ s}^{-1}$) was enhanced by about 3-fold compared to the value of randomly oriented films (~4.5 X 10⁻² cm² V⁻¹ s⁻¹). Our group 107 recently established a flowdirected molecular assembly mechanism that guided interfacial alignment of blade-coated DPP2T-TT thin films. We found that highly aligned fibrils were formed at the top surface, with the long axis of the fibril along the coating direction; in contrast, the fibers were weakly orthogonal to the coating direction or completely lost in the bulk depending on the film thickness (Figure 8b). We proposed that the difference in orientational ordering between the top surface and the bulk film is caused by distinct extension- and shear-dominant flow regimes. Near the solution-air interface, extensional flow develops due to an evaporative flux gradient. This extensional flow induces a net torque onto the anisotropic fibrils, leading to parallel alignment of the fiber long axis along the coating direction. In contrast, the bulk of the ink solution is under a shear-dominant regime. In this case vorticity plays a dominant role in guiding the polymer fibers to align orthogonal to the

coating direction in the bulk. Xu and Bao et al. ⁷² recently demonstrated highly stretchable polymer semiconducting films printed using solution shearing with a patterned microtrench coating blade which was designed to effectively generate a strong unidirectional flow field (Figure 8c). Combined with the nanoconfinement effect through the "CONPHINE" method, the authors were able to control multiscale ordering across the molecular, meso-, and macroscales for simultaneous improvement of electrical performance and polymer chain dynamics for mechanical stretchability. We refer the readers to our recent reviews on understanding and engineering the fluid flow for further in depth discussions. ^{62,63}

4.1.2. Printing Regime Dependency. The printing regimes laid out in Section 3.2.1 have a profound impact on the morphology of printed conjugated polymer films; the ideal printing speed in MGP for enhancing aggregation and alignment is typically neither extremely slow nor extremely fast but somewhere in between. Shaw and Bao et al. 60 reported a "critical" shear speed where a highest degree of polymer chain alignment was observed among poly-(diketopyrrolopyrrole-terthiophene) (PDPP3T) films printed at a wide range of printing speeds (Figure 9a). At the critical shear speed of 0.2 mm/s, a maximum optical dichroic ratio of ~7 was achieved, indicating that the polymer chains were highly aligned along the shearing direction. Below the critical speed, shear strain was not sufficient in the polymer chain alignment. Beyond the critical speed, no further enhancement in alignment was obtained despite a significant increase in the shear strain experienced. In their following study,⁷¹ they showed that the film with the highest dichroism did not correspond to the most crystalline film, proposing shear induces the alignment of both the amorphous and crystalline regions. The authors also suggested three printing regimes, the shear-dominate, disorder-dominate, and LL regimes separated by two transition points: the classical fluid mechanical transition between the evaporation and LL regimes and a transition related to the crystallization rate. Each regime is indicated by a different color in Figure 9a. Another work by Wang, Facchetti, and Marks et al.⁶¹ also reported an optimal printing regime to reach a high degree of polymer aggregation as well as backbone alignment. They used natural brush printing to control backbone alignment and aggregation in several different conjugated polymer systems and demonstrated how these resulted films influence the charge transport property. The four conjugated polymer systems studied were P3HT, P(NDI2OD-T2), poly[4,8-bis(5-(2-ethylhexyl)thiophen-2-yl)benzo-[1,2-b;4,5-b']dithiophene-2,6-diyl-alt-(4-(2-ethylhexyl)-3-fluorothieno[3,4-b]thiophene-)-2-carboxylate-2-6-diyl)] (PBDTT-FTTE), and poly(3,4ethylenedioxythiophene):poly(styrenesulfonate) (PE-DOT:PSS) (molecular structures shown in Figure 9b, top). In the intermediate printing speeds $(1-3 \text{ mm s}^{-1})$, both optical dichroism and aggregation fraction (or relative degree of aggregation) of all polymer films were maximum (except the optical dichroism of PEDOP:PSS due to its optical transparency) (Figure 9b, bottom). The resulted films deposited in this regime yielded enhanced charge carrier mobilities of 0.21 cm 2 V $^{-1}$ s $^{-1}$ for P3HT, 2.3 cm 2 V $^{-1}$ s $^{-1}$ for N2200, and 0.044 $\mbox{cm}^2\mbox{ }\mbox{V}^{-1}\mbox{ }\mbox{s}^{-1}$ for PBDTT-FTTE and a DC conductivity of 3460 S cm⁻¹ for PEDOT:PSS. This is attributed to shear-induced polymer chain extension, which can be more easily packed to yield nanofibril aggregates as to enhance charge transport.

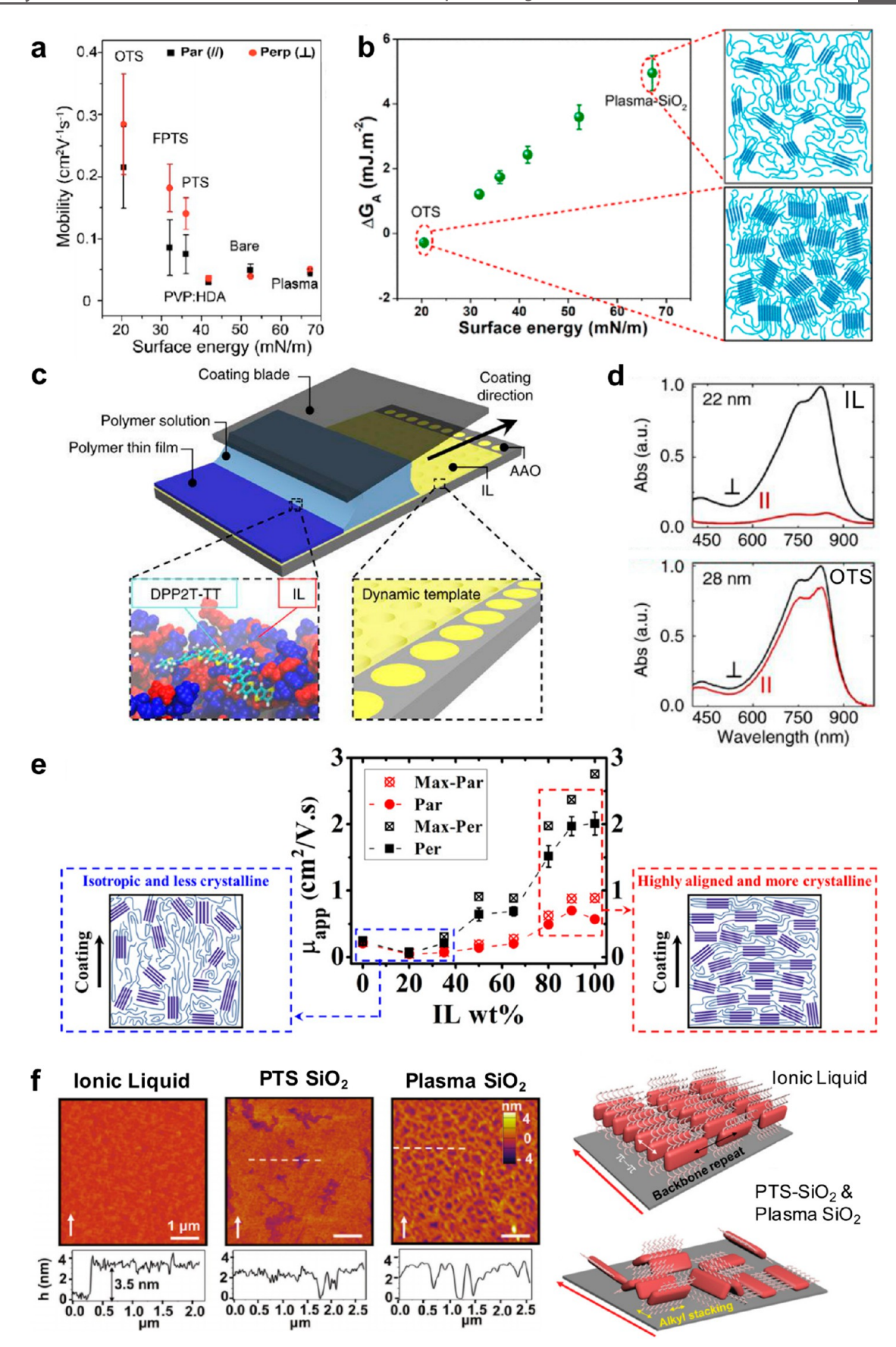


Figure 10. Substrate modification for morphology control. (a) Hole mobility of DPP2T-TT films printed on substrates with varying surface energy. (b) Substrate surface-energy dependent excess free energy per surface area and illustration of thin film morphology on high and low surface energy substrates. (a, b) Reproduced with permission from ref 114. Copyright 2018 American Chemical Society. (c) Schematic of meniscus-guided

Figure 10. continued

coating setup with dynamic template consisting of ionic liquid infiltrated with anodized aluminum oxide (AAO) substrate. (d) Normalized absorption spectra of polarized UV—vis spectroscopy of DPP2T-TT films printed on IL and OTS. The symbol \parallel (\perp) denotes that the polarizer is parallel (perpendicular) to the coating direction. (c, d) Reproduced from ref 84. "Dynamic-template-directed multiscale assembly for large-area coating of highly-aligned conjugated polymer thin films" by Mohammadi, E., et al. is licensed under CC BY 4.0. To view a copy of this license, visit http://creativecommons.org/licenses/by/4.0/. (e) Apparent hole mobility of DPP-BTZ films printed on the ion gel parallel and perpendicular to the coating direction as a function of IL percent in the polymer matrix. The inset is a cartoon representation of polymer mesoscale morphology showing highly crystalline and highly aligned polymer fibers coated on IL-rich gels. Reproduced with permission from ref 85. Copyright 2019 American Chemical Society. (f) Film morphology and molecular packing of DPP2T-TT monolayers printed on ionic liquid (dynamic template) and PTS-SiO₂ and Plasma SiO₂ (static substrates). Reproduced with permission from ref 116. Copyright 2020 John Wiley and Sons.

To understand how these regimes affect the meniscus flow field and the resulting morphology of printed conjugated polymer films, our group carried out a combined simulation and experimental study. 94 We have demonstrated that PII-2T films printed over a large range of speeds resulted in vastly different morphologies from the molecular to device scale. UV-vis and Raman spectroscopy (Figure 9c) and AFM (Figure 9d) were employed to reveal distinct molecular conformations and consequential morphologies of the printed films. In the evaporation regime $(0.1-0.5 \text{ mm s}^{-1})$, the conjugated polymer exhibited a torsional conformation and assembled into twinned domains aligned perpendicular to the printing direction. The GIXD dichroic ratio (R_{GIXD}) for the films printed in the evaporation regime was ~0.64. In the transition regime (1-2 mm s⁻¹), the polymer chains became planarized, leading to highly aligned films parallel to the printing direction ($R_{GIXD} = 11.4$). In the LL regime (>3 mm s^{-1}), domains without global alignment ($R_{GIXD} = 1.96$) but with local twinning were observed. Our simulation results rationalized that the transition regime is ideal for enhancing conjugated polymer planarization and alignment by combining a high strain rate with a short residence time (see details in Section 3.2.1). The high strain rate induced polymer conformation change and fibril alignment, when the short residence time prevented the polymer conformational relaxation and aggregate orientational relaxation. In contrast, the low strain rate in the evaporation regime allowed the polymer to adopt a near-equilibrium torsional conformation. In the LL regime, while the maximum strain rate is higher than in the transition regime, the flattened polymer backbone partially relaxed when the polymer travelled through a prolonged liquid film of low strain rate before solidification. For aligned films printed in the transition regime, the field-effect mobility reached 1.1 cm² V⁻¹ s⁻¹, compared to 0.39 and 0.41 cm² V⁻¹ s⁻¹ for the films printed in the evaporation and LL regime, respectively. We also observed distinct differences in charge transport anisotropy across the three printing regimes (Figure 9e). The field-effect mobility for the transition regime is highly anisotropic, which is 4-fold higher along the printing direction than the transverse direction indicating favorable charge transport along the polymer backbone. In comparison, films from the evaporation and LL regimes exhibit isotropic charge transport consistent with their low degrees of alignment. We proposed a molecular assembly mechanism that flow extinguishes a lyotropic twist-bend mesophase upon backbone planarization, leading to the observed morphology and electronic structure transitions (Figure 9f).

4.2. Surface Modification. The choice of substrate for fabricating conjugated polymer thin films has a profound impact on the film morphology, molecular packing, alignment, degree of crystallinity, orientation, and ultimately device

performance. Thus, there is an intense push for investigating novel substrates that result in desired film properties. The substrates used during solution processing of polymer films can provide sites for heterogeneous nucleation; hence, their properties may dictate the properties of the film near the interfaces or even throughout the bulk of the film. Further, substrate-solution interactions influence the dynamic contact angle during printing, thereby modulating the solvent evaporation rate and printing regimes. The importance of specific substrate—polymer interactions, ^{108,109} surface topology, ^{110,111} and lattice matching in guiding the multiscale morphology 112 of polymers during assembly has been realized in numerous studies. We would like to direct the readers to our recent review for the fundaments and a comprehensive summary of the interface-directed assembly. 63 In this section, we will highlight the most recent works by our group and related works by others on the impact of surface energy and surface dynamics on polymer crystallinity and alignment.

Several groups have demonstrated that the substrate surface energy plays a major role in determining film orientation, crystallinity ,and device performance. ^{113–115} For instance, Guo and Lee et al. 113 realized an increase in alignment and enhanced mobility of solution-sheared poly(diketopyrrolo[3,4c]pyrrole-co-thieno[3,2-b]thiophene) (PBDT-co-TT) films on low surface energy octadecyltrichlorosilane (OTS) coated SiO₂ compared to those on relatively higher surface energy bare silicon at a wide range of printing speeds (0.1 to 2 mm s⁻¹). At the printing speed of 1.5 mm s⁻¹, the UV-vis dichroic ratios of the polymer were 1.2 and 1.6 on bare SiO₂ and OTS-SiO₂, respectively. Similarly, in our study 114 involving DPP2T-TT films printed on substrates over a wide range of surface energies (γ_{SV} = 20.5 to 67.2 mN m⁻¹), we observed an increase in the degree of crystallinity and drastic enhancement of polymer alignment on utilization of low surface energy substrates. For instance, the films had a 5-fold enhancement in alignment with an edge-on $\pi-\pi$ stacking dichroic ratio of 5.2 for films on OTS-SiO₂ ($\gamma_{SV} = 20.5 \text{ mN m}^{-1}$) and ~1 in the case of plasma treated ${\rm SiO_2}$ ($\gamma_{\rm SV}$ = 67.2 mN m⁻¹). This enhancement in film morphology was reflected in an improved electronic performance of the polymer films. We chose top gate device geometry with the same gate dielectric across all conditions to eliminate the direct impact of the substrate surface chemistry on the device performance. Measured along the alignment direction of the polymer backbone, the films printed on OTS-SiO₂ showed a mobility of 0.29 cm² V⁻¹ s⁻¹, almost 6-fold higher than that of films printed on plasma treated SiO2, purely owing to differences in film morphology (Figure 10a).

The mounting evidence of the viability of varying surface energy to modulate polymer crystallization and alignment led us to develop a generic free energy model for 2D

heterogeneous nucleation that quantitatively elucidates the mechanism behind this modulation.

114 Our model is based on the assumption that substrate surface energies dictate thin film morphology by modulating the free energy barrier to heterogeneous nucleation. The total free energy change due to nucleation ($\Delta G_{Nucleation}$) is composed of a volume term which drives the nucleation and an unfavorable surface term which is the penalty for forming a new surface, expressed as

$$\Delta G_{Nucleation} = -V\Delta G_V + A\Delta G_A \tag{10}$$

where ΔG_V is the excess free energy per volume between the bulk solid and the solvated solute and ΔG_A is the excess free energy per surface area between the surface and the bulk of the nucleus. While ΔG_V is independent of the substrate, ΔG_A considers the pairwise interfacial free energies among the nucleus, substrate, and solvent and can be written as

$$\Delta G_{A} = \gamma_{polymer-solvent} + \gamma_{substrate-polymer} - \gamma_{substrate-solvent}$$
(11)

which, when combined with the equation-of-state, yields

$$\Delta G_{A} = 2[\gamma_{polymer} - \sqrt{\gamma_{solvent}\gamma_{polymer}}(1 - \beta(\gamma_{solvent} - \gamma_{polymer})^{2})$$

$$- \sqrt{\gamma_{substrate}\gamma_{polymer}}(1 - \beta(\gamma_{substrate} - \gamma_{polymer})^{2})$$

$$+ \sqrt{\gamma_{substrate}\gamma_{solvent}}(1 - \beta(\gamma_{substrate} - \gamma_{solvent})^{2})]$$
(12)

where γ_i is interfacial free energy between component i and air and β is an empirical constant unique to substrates and can be determined using the least-squares regression method. For the polymer—solvent system used in our study, we determined that lower surface energy results in lower free energy of nucleation, $\Delta G_{Nucleation}$, which was ultimately manifested on the enhanced polymer alignment and higher mobility (Figure 10b). However, we note that lower surface energy may not necessarily lead to enhanced morphology in all cases as it depends on the solvent used as implied in our model.

While modifying the surface energy of the substrates can enhance the ordering of the polymers, their adsorption on solid substrates usually restricts their diffusion and freedom to orient and crystallize in more efficient and ordered packing. We developed dynamic interfaces that allow surface reconfigurability during polymer assembly on top, which led to drastically enhanced ordering not attainable using static surfaces. 84,86,11 Besides enhanced morphology, an additional advantage of liquid surfaces is that the films printed on top can be easily transferred to a desired surface/dielectric including flexible substrates. The first generation of the dynamic templates was fabricated by infusing an imidazolium based ionic liquid (IL), 1-ethyl-3-methylimidazolium bis(trifluoromethylsulfonyl)imide ([EMIM]-[TFSI]), in nanoporous anodized aluminum oxide. The nanoporous media retain IL during meniscusguided coating, allowing us to successfully fabricate films of DPP2T-TT and PII-2T (Figure 10c).84 Compared to the films directly coated on OTS functionalized SiO2, the DPP2T-TT films printed on the IL and subsequently transferred to the OTS substrate had a drastic 4-fold ($3.0 \text{ vs } 0.8 \text{ cm}^2 \text{ V}^{-1} \text{ s}^{-1}$) and 2-fold (2.7 vs $1.4 \text{ cm}^2 \text{ V}^{-1} \text{ s}^{-1}$) rise in hole mobility of the best performing device, parallel (along $\pi-\pi$ stacking) and perpendicular (along polymer backbone) to the coating direction, respectively. We attributed this improvement to a high degree of alignment and crystallinity for the films prepared on the IL as measured by UV-vis spectroscopy, GIXD, and transmission electron microscopy (TEM). For

instance, polarized UV-vis spectroscopy showed that ILprinted films exhibited a high dichroic ratio, whereas a significantly lower dichroic ratio was observed for OTS-SiO₂ coated polymer films (Figure 10d). This clearly demonstrated a high degree of polymer alignment induced by the IL compared to OTS-SiO₂. Molecular dynamics simulations revealed the mechanism of dynamic-templates-enhanced crystallization: strong interactions between the cations in the IL and the electronegative oxygen atoms in the polymer backbone led to a several-fold increase in polymer concentration near the IL-solution interface, only when the IL molecules were allowed to move. The enrichment of polymer near the dynamic template decreases the free energy barrier for nucleation, while the surface reconfiguration of the IL surface further assists in the ordering of the polymer backbone by constantly exposing favorable binding sites for polymers to adsorb.

To further impart the tunability of surface dynamics and chemical composition, we designed ion-gel templates composed of an elastic polyvinylidene fluoride-co-hexafluoropropylene (e-P(VDF:HFP)) polymer matrix infused with an [EMIM][TFSI] IL.85 Varying the weight percent of the IL afforded a large modulation of the glass transition temperature (and thus the template dynamics) of the ion gel over 70 °C. The complementary chemistries of the IL and polymer matrix of the ion gel further produced a synergistic templating effect: the IL interacts with the backbone of the conjugated polymer through an ion- π interaction while the e-P(VDF:HFP) interacts the alkyl chain of the conjugated polymer through a van der Waals interaction. As a result, films of diketopyrrolopyrrole-benzothiadiazole-based copolymer (DPP-BTz) and PII-2T printed on the IL-polymer matrix showed superior morphology compared to those printed on either component alone. At optimized conditions (80-90 wt % of IL), the ion gel printed DPP-BTz films had a 55 times higher in-plane π - π stacking dichroic ratio and 49% higher relative degree of crystallinity compared to those printed on neat e-P-(VDF:HFP) surfaces. This led to enhancement of maximum hole mobilities along the π - π stacking and the backbone by a factor of 4 and 11, respectively (Figure 10e). We further validated the importance of multivalent interactions in templating conjugated polymers by designing dynamic surfaces with three components of complementary chemistries: (i) e-P(VDF:HFP), (ii) [EMIM]-[TFSI], and (iii) hydrogen bonded liquid ethylene glycol.⁸⁷ We observed that, in the presence of all three components in the template, the relative degree of crystallinity and macroscopic alignment of the polymer films were enhanced by 50-100% and 200-500%, respectively, compared to those templated by a single component alone; the absence of any one of the components resulted in decreased ordering of the polymer films. Interestingly, isothermal titration calorimetry (ITC) measurements also showed that the ternary system had a 45% increase in the heat of adsorption with the polymer compared to neat substrates. This corroborates with our assumption that the increased template-polymer interaction due to the introduction of complementary binding sites acts to enrich the conjugated polymer near the dynamic template and decrease the nucleation barrier by a larger extent.

Such strong cooperative multivalent interactions enabled by template dynamics further led to printing of highly ordered 2D monolayer films (\sim 2.5-3.5 nm thick) of conjugated polymers by promoting 2D crystallization on dynamic templates. ¹¹⁶ The

DPP2T-TT 2D monolayer films deposited using dynamictemplate-assisted MGC exhibited a fractal dimension of 2 and 100% coverage without voids nor discontinuities; strong and anisotropic edge-on π - π stacking was also observed (Figure 10f). In contrast, monolayers deposited on reference static substrates, plasma treated SiO₂, and trimethyl(phenyl)silane (PTS) functionalized SiO₂ exhibited 1D network morphology with coverage of only 69% and 89% and fractal dimension of 1.33 and 1.48, respectively. Further, no $\pi - \pi$ but alkyl stacking peak was found via GIXD. Due to the poor morphology, these monolayers coated on static substrates also did not show any charge transport properties. In comparison, the 2D monolayers coated on the dynamic template did afford measurable charge carrier mobilities. Besides facilitating 2D monolayer formation, we further applied the dynamic templating approach to controlling out-of-plane orientation of conjugated polymers as to largely modulate surface doping effect.

Liquid surfaces, such as hydrogen-bonded and ionic liquids, have been utilized in several other studies as substrates during solution processing. 118-122 For instance, Yang, Liu, Chi, and Zhang et al. 118 utilized water as a substrate to deposit films of several donor-acceptor polymers such as poly[2,5-bis(2octyldodecyl)pyrrolo[3,4-c]pyrrole-1,4(2H,5H)-dione-3,6diyl)-alt-(2,2';5',2";5",2" -quaterthiophen-5,5" -diyl)] (PDPP4T) by drop-casting the polymer solution on water. The films thus formed demonstrated densely packed and highly crystalline films with predominantly edge-on orientation. Such an orientation was attributed to the tendency of the hydrophobic side chains to minimize the contact area with water. This led to an increase in average charge carrier mobility by almost an order of magnitude (0.8 to 8.15 cm² V⁻¹ s⁻¹) compared to films spin-coated on plasma treated SiO₂/Si substrates. In these studies, whether and how liquid substrates participate in the polymer assembly process remain to be further elucidated.

4.3. Tuning Assembly Pathways. Assembly pathways of conjugated polymers are very sensitive to processing, and controlling the pathways can offer large modulation of their multiscale morphology to ultimately enhance device performance. First of all, conjugated polymers can have various chain conformations from random coil, collapsed coil, worm-like cylinder to rigid rods depending on intrinsic molecular structures, and polymer-solvent interactions in a given processing condition. This variety can critically impact the nature of the solution state, leading to fully dispersed molecular solutions or solutions containing preassembled structures. In conjugated polymers, the main intermolecular forces are $\pi - \pi$ interactions between the backbones and dispersion forces between the alkyl side chains. Such interactions often result in the formation of preaggregates and/or liquid-crystal (LC) mesophases in solutions. In particular, D-A copolymers can easily form preaggregates or mesophases because of their efficient intramolecular charge transfer from donor to acceptor moieties, resulting in planarization of the backbone and strong intermolecular interactions. In this section, we discuss two main types of conjugated polymer assembly pathways recently studied: (i) preaggregation mediated assembly and (ii) LC-mediated assembly pathways. Key aspects on tuning the assembly pathways include how various factors impact the assembly pathways from the solution to the thin films, how the assembly pathways define the multiscale thin film morphology, and how the pathways can be tuned by design. While these questions

still remain largely unanswered, recent advances have begun to reveal possible assembly pathways of conjugated polymers and their structural characteristics across length scales.

4.3.1. Preaggregation Mediated Assembly Pathway. Preaggregation or polymer aggregation in solution prior to film deposition has been explored to modulate properties of conjugated polymer films. The ordered preaggregates in solution are believed to self-seed the further aggregation and alignment of polymer chains as they crystallize into thin films. 123-125 Moreover, these aggregates can inhibit formation of amorphous regions and enhance the growth of largerordered grains in the films. 125 Several groups have realized enhanced polymer assembly and charge transport properties using preaggregated solutions. For instance, Luzio and Caironi et al. reported a high degree of orientational order in thin films of P(NDI2OD-T2) spin-coated from toluene compared to those in weakly aggregating solvent systems. 126 This resulted in a saturated mobility of 0.73 cm² V⁻¹ s⁻¹ in the films, which is more than 36 times higher than the mobility of the films prepared using a weakly aggregating chloronaphthalene (CN) and chloroform (CF) mixture (80:20 by volume). Choi and Reichmanis et al. reported a 4-fold rise in the average hole mobility in P3HT films fabricated from a solution subjected to treatments (nonsolvent addition and ultrasonication) that resulted in rod-like preaggregates in the solution as compared to the untreated counterparts. Li, Müllen, and Pisula et al. demonstrated tuning of the preaggregation fraction and resultant orientational ordering. Gradual addition of 1,2,4trichlorobenzene (TCB) to the preaggregated CF solution of difluorobenzothiadiazole-quarterthiophene-based copolymer reduced the aggregation fraction as observed through UVvis spectroscopy. The preaggregation dictated the orientation of the polymer in films with strongly (weakly) aggregating solution preferring edge-on (face-on) orientation. As a result, this change of aggregation degree as well as molecular orientation largely modulated the electronic performance of the films fabricated; for instance, the hole mobility of 2 cm² V⁻¹ s⁻¹ in polymer films from the pure CF solution was reduced to 0.0846 cm² V⁻¹ s⁻¹ from 20 CF:1TCB mixed solution and further decreased to 10⁻⁶ cm² V⁻¹ s⁻¹ from pure TCB solution with a reduction of the preaggregate fraction.

The mechanism of polymer preaggregation in solution has been widely studied. One of the most accepted models is a temperature-induced disorder-order transition which states that highly disordered polymers at high temperature in solution first expand and then begin to aggregate as it is cooled; upon a further decrease in temperature the polymer chains in the aggregated phase further planarize. 50 The shape, size, and extent to which the preaggregation of polymer occurs in solution is affected by several factors. The relative interaction between the polymer and the solvent is one of the most important. It is widely accepted that utilization of a solvent in which the polymer-solvent interaction is less favorable than the polymer-polymer interaction, i.e., "poor solvent", enhances preaggregation. While this is true in the case of polymers like P3HT, the presence of large π -plane and strong π - π interaction in D-A polymers leads them to aggregate even in the dilute solution of a "good solvent". Utilizing SANS in combination with UV-vis spectroscopy, Zheng, Zou, Wang, and Pei et al. determined that a benzodifurandione-based oligo(p-phenylenevinylene) (BDOPV)-based conjugated polymer, BDOPV-2T, adopts a rod-like 1D aggregate in the good solvent 1,2-dichlorobenzene

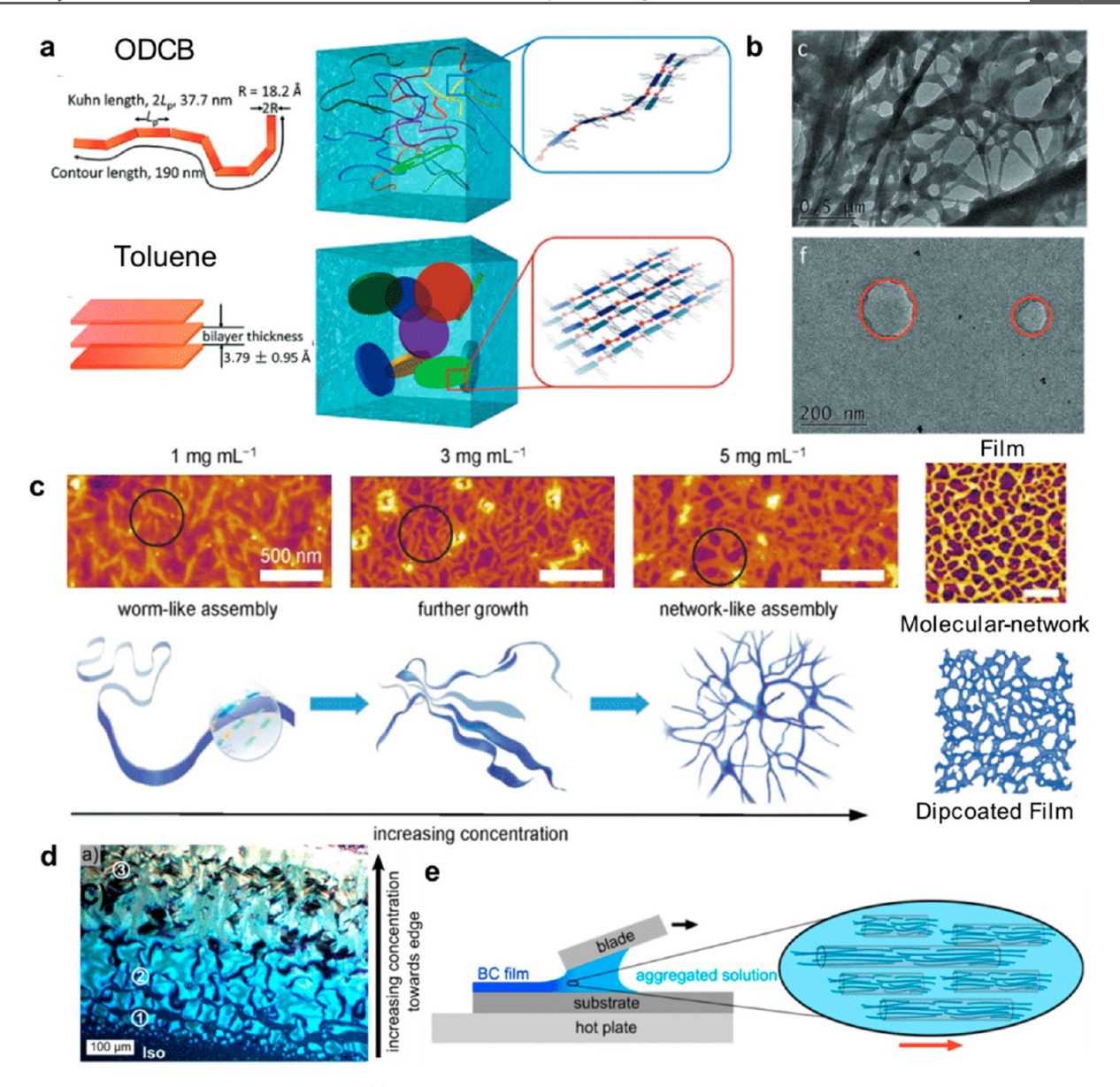


Figure 11. Polymer assembly via preaggregation. (a) Schematic diagram of the worm-like chain model and lamellar model for BDOPV-2T polymer in ODCB and toluene, respectively (left), and proposed structure of polymer aggregates in the corresponding solution (right). (b) TEM images of BDOPV-2T freeze-dried from solution in ODCB (top) and toluene (bottom). (a, b) Reproduced with permission from ref 129. Copyright 2017 John Wiley and Sons. (c) AFM height images of $F_4BDOPV-2T$ freeze-dried from chloroform at different solution concentrations as well as dipcoated at a 200 μ m s⁻¹ speed from 1 mg m L⁻¹ solution in chloroform, along with a schematic of the corresponding proposed assemblies. Reproduced with permission from ref 134. Copyright 2018 John Wiley and Sons. (d) Polarized optical microscopy image of highly preaggregated P(NDI2OD-T2) solution in chlorobenzene sandwiched between glass slides resembling features of chromonic liquid crystals. (e) Schematic of P(NDI2OD-T2) fiber and chain orientation during solution coating. (d, e) Reproduced with permission from ref 106. Copyright 2019 American Chemical Society.

(ODCB) because of an enhanced dispersive interaction between the polymer and the solvent which causes the polymer chains to extend as postulated by the authors (Figure 11a). 129 In contrast, "bad solvents" such as toluene formed 2D large aggregates containing lamella-like packing that already exhibited $\pi-\pi$ stacking between the polymer backbone while in the solution phase to reduce polymer–solvent interaction. 129 The supramolecular structure of the polymer in the solution was retained in solid thin films spin-coated from the same solution, which is attributed to the strong interaction between the aggregates and the substrate (Figure 11b). The degree of aggregation is also effected by regioregularity. Gross and Ludwigs et al. tuned the regioregularity of P(NDI2OD-

T2) by changing the ratio of 2,6- and 2,7-linkages and realized that increasing 2,7-linkages resulted in a decrease of preaggregation in toluene, a poor solvent, possibly due to lowered intermolecular interactions between the polymer chains. Studies have also indicated that polymers with more planar backbones tend to favor aggregate formation as a result of stabilized $\pi-\pi$ stacking and van der Waals interactions between the polymer chains. Using temperature dependent H NMR and UV—vis spectroscopy, Matsidik, Caironi, and Sommer et al. showed that a bifuran analogue of PNDIT2, PNDI-Fu2-C16, with a more planar backbone, had stronger preaggregation than PNDI-T2-C16 which has a higher backbone torsional angle. When spin-casted into thin films,

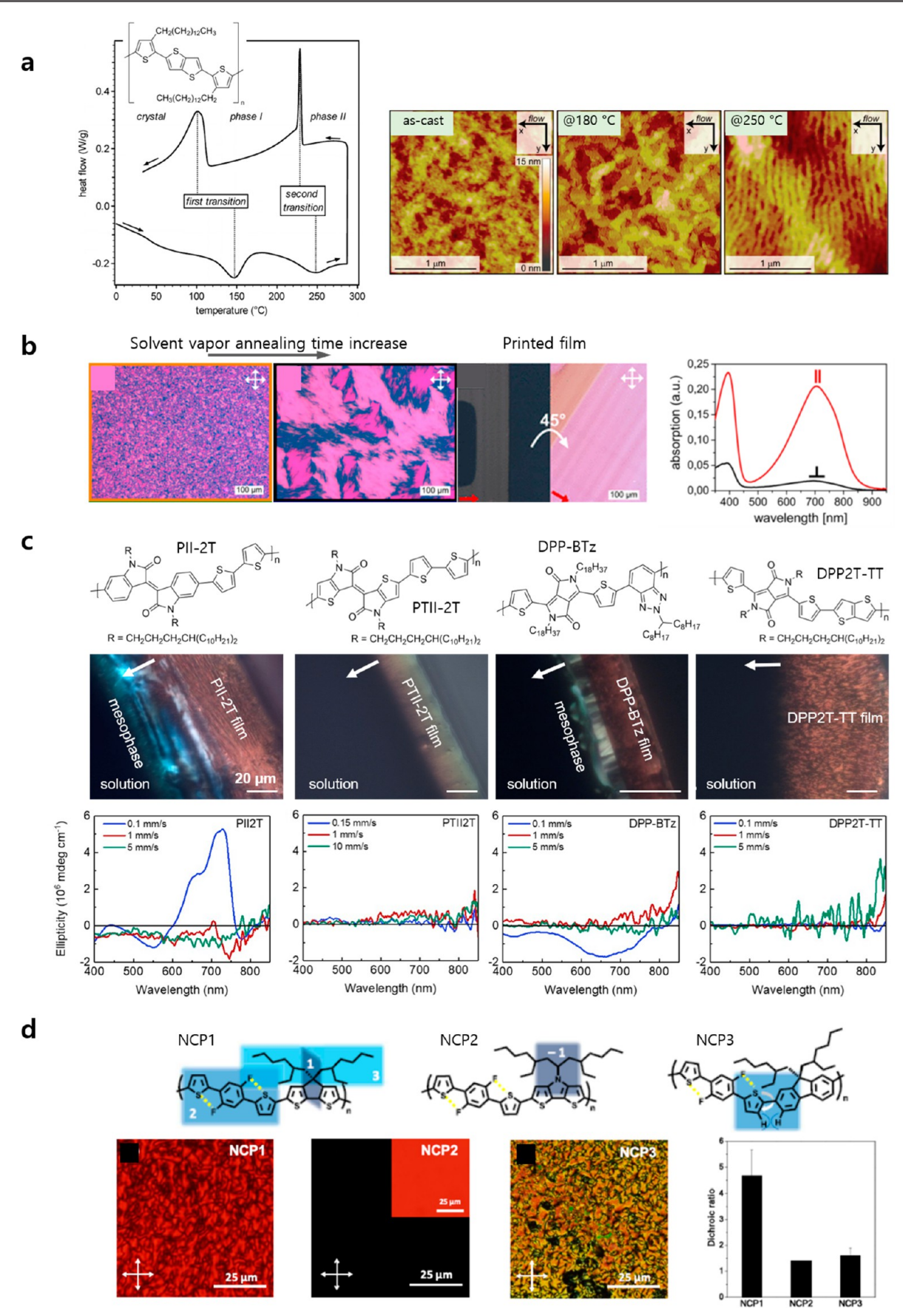


Figure 12. LC phase mediated morphology controls. (a) Differential scanning calorimetry of pBTTT, exhibiting two distinct phase transitions (left). Thermal annealing effect on pBTTT films printed by flow coating, exhibiting each featureless, terraced, and oriented ribbon topology at the temperature indicated (right). Reproduced with permission from ref 148. Copyright 2009 American Chemical Society. (b) Polarized optical

Figure 12. continued

micrograph of P(NDI2OD-T2) films of increased crystal domain size upon solvent vapor annealing and of printed aligned films and corresponding polarized UV—vis spectra. Reproduced with permission from ref 106. Copyright 2019 American Chemical Society. (c) Chemical structure of two pairs of twisted D—A polymers (PII-2T and DPP-BTz) and their planar counterparts (PTII-2T and DPP2T-TT) (top). CPOM images of the solution- to solid-state phase transition in a receding meniscus driven by solvent evaporation of each polymer (middle). CD spectra of each polymer films comparing three regimes—evaporation regime (0.1 mm/s), transition regime (1 mm/s), and Landau—Levich regime (5 mm/s) (bottom). From ref 94. Copyright Park, K.S. and Kwok, J.J., et al., some rights reserved; exclusive licensee American Association for the Advancement of Science. Distributed under a CC BY-NC 4.0 License (http://creativecommons.org/licenses/by-nc/4.0/). (d) Conjugated polymer design with an out-of-plane side-chain linker (1), a main chain planarity (2), and a side-chain design (3) (NCP1) and its variants (NCP2 and NCP3) (top). CPOM images of concentrated solutions (over 200 mg m L⁻¹) and dichroic ratios of corresponding films (bottom). Reproduced with permission from ref 154. Copyright 2019 American Chemical Society.

PNDI-Fu2-C16 also showed higher anisotropy observed through UV-vis spectroscopy and a significantly lower (0.35 nm) π - π stacking distance compared to that of PNDI-T2-C16 (0.39 nm). The stiffness of the polymer backbone can also determine the type of aggregate in solution. Ziffer, Jen, and Ginger et al. reported that the stiffer regioregular analogue of poly[4,8-bis(5-(2-ethylhexyl)thiophen-2-yl)benzo[1,2-b:4,5b']dithiophene-co-3-fluorothieno[3,4-b]-thiophene-2-carboxylate] (PTB7-Th) exhibited J-aggregate-like behavior (intrachain dominating exciton coupling) while the flexible counterpart showed H-like characteristics (interchain dominating exciton coupling). Besides the molecular design, UV-vis irradiation ¹³³ and ultrasonication ¹²⁷ have also been employed to enhance preaggregation in polymer solution. The proposed mechanism is that aggregation is enhanced by photoexcitation during UV-vis irradiation and by the high strain rate created during bubble collapse by sonication.

While numerous studies have indicated the positive influence of preaggregates on thin film assembly, the exact process of how the preaggregates transform into solid films is still open to speculation. Recently, Yao, Lei, and Pei et al. proposed a multiscale assembly process of conjugated polymers, where strong π – π stacking between polymer chains, facilitated by the use of poor solvents, results in worm-like aggregates that elongate with increasing solution concentration and ultimately grow into a network-like structure in concentrated solution during evaporative assembly (Figure 11c). 134 Through this assembly pathway, large-area monolayer films of an n-type semiconductor, tetra-fluorinated BDOPVbithiophene polymer, F₄BDOPV-2T, with interconnected fiber networks were successfully dip-coated using CF and DCM solvent mixture systems; the SANS data along with visualization of the freeze-dried solution at different concentrations confirmed the presence and growth of polymer preaggregates in the solution phase. In contrast, use of "better" solvents such as chlorobenzene resulted in noncontinuous films with discrete polymer fibers.

Besides forming network-like secondary aggregates, preaggregates in solution can also form liquid crystals upon increasing concentration on their way to solid film formation. In strongly aggregating polymeric systems like P(NDI2OD-T2), several reports have suggested the presence of LC mesophases, ^{106,126,135,136} in some cases resembling textures of chromonic liquid crystals (Figure 11d). ¹⁰⁶ In solution-processed film deposition of these polymers, these aggregates are assumed to initiate a transformation into LC mesophases with solvent evaporation, leading to the formation of highly oriented regions upon application of a shear force (Figure 11e) or magnetic field. ^{106,125} The influence of liquid crystals on film

morphology and electronic properties is described in detail in the following section.

4.3.2. LC Phase Mediated Assembly Pathway. An LC is a thermodynamically stable state existing between the liquid and solid phase, which exhibit both the fluidity of liquids and the crystallinity of solids. LCs are mainly divided into two basic classes, thermotropic and lyotropic phases depending on what fundamental parameter induces the LC phase. Thermotropic LCs exhibit a phase transition induced by temperature or pressure, where orientational entropy loss during LC phase formation is compensated by the enthalpy gain. On the other hand, lyotropic LCs are observed when the particle concentration reaches a critical level. Colloidal suspensions of geometrically anisotropic particles have often been observed to produce LC phases. The origin of this LC phase emergence has been elucidated by the classical theory developed by Onsager. 137 With an assumption of rigid rods and high aspect ratio particles, an isotropic-to-nematic transition arises from an orientational entropy decrease due to overlapping excluded volume of the particles above a critical concentration. The critical volume fraction to induce an isotropic-to-nematic transition scales with the aspect ratio (diameter/length) of rodlike particles, which decreases with an increasing length of particles. Tremendous progress has been made following this cornerstone study to add to the knowledge of LC phase origin and behavior being affected by various parameters, including molecular shape, aspect ratio, volume exclusion interaction, amphiphilicity, attractive interaction, persistence length, etc. 138-140 As previously discussed in Section 2.1, conjugated polymers have highly anisotropic molecular structures with high backbone rigidity characterized by persistence length (l_n) . In some cases, the l_v of a conjugated polymer chain or aggregate exceeds the contour length and can thus be treated as a rod-like particle. In this case the critical volume fraction for the isotropic-to-nematic transition can be predicted by d/l_p , where d is the chain/aggregate diameter. ^{141,142} The prediction was further improved by considering orientational coupling between backbone segments. 143 Other than anisotropic molecular shape and volume exclusion interactions, anisotropic attractive interactions and/or amphiphilic interactions (π – π vs side chain interactions) can also facilitate LC phase formation.

Early works on controlling the molecular arrangement of conjugated polymers involved thermotropic LC phases that were aligned on a topological template or mechanically rubbed in a molten state. Several conjugated polymers such as poly-9,9'-dioctylfluorene-co-bithiophene (F8T2), poly(9,9-dioctylfluorene-co-benzothiadiazole) (F8BT), poly-3,3 $^{\prime\prime\prime}$ -dialkylquaterthiophene (PQT), and poly-2,5-bis(3-alkylthiophen-2-yl)thieno[3,2b]thiophenes (pBTTT) have been reported to exhibit a thermotropic LC phase at a temperature range of

100–250 $^{\circ}\text{C.}^{144-148}$ Such character enables manipulation of the crystallite domain size and molecular alignment upon an appropriate thermal treatment. Understanding molecular behaviors in a LC phase has permitted the achievement of a higher level of molecular orientation. DeLongchamp et al. 148 found two distinct thermally induced phase transitions of pBTTT (Figure 12a, left). Accordingly, the morphology of blade-coated pBTTT films can be controlled by tuning the annealing temperature: annealing to the first transition led to the formation of large terrace-shaped crystals, and annealing to the second transition resulted in highly aligned ribbons (Figure 12a, right). The authors explained that two distinct phase transitions resulted from the melting of alkyl side chains followed by backbone melting. The formation of aligned ribbons was attributed to a mobile nematic mesophase which arises from backbone melting and can be aligned along the "seed" initially oriented by flow.

While thermotropic LCs of conjugated polymers have long been studied, lyotropic LCs are gaining interests in recent years due to its direct relevance to solution processing. Lyotropic liquid crystals are highly relevant to solution printing since the ink solution traverses the entire concentration range from the initial (semi)dilute solution to the solid state owing to continuous solvent evaporation. Therefore, understanding and tuning of the lyotropic phases of conjugated polymers can enable control over the morphology of printed polymer films. An appropriate solvent choice is required to induce the LC phase by promoting intermolecular interactions while at the same time inhibiting massive aggregation. P(NDI2OD-T2) has showed a variety of solution phase behaviors and film morphologies depending on the solvent used. 126 In particular, a toluene solution exhibited a high degree of preaggregation, which yielded large birefringent domains (even millimeter-sized) in the spin-coated film. Trefz and Ludwigs et al. 106 recently reported lyotropic LC behavior of P(NDI2OD-T2) in chlorobenzene (CB) at high concentrations. The authors demonstrated that the presence of the LC phase is beneficial for tuning the morphology as the polymer crystals increased in size upon solvent vapor annealing possibly mediated by the lyotropic LC phase (Figure 12b). The authors also used a blade coating method for improving polymer alignment mediated by this LC phase. The polymer film printed at 1 mm s⁻¹ resulted in a high degree of alignment with an optical dichroic ratio of 18 and charge transport anisotropies up to 14, in which polymer backbone and fiber long axis were oriented parallel to the printing direction. In fact, it was commonly found that solution shearing leads to unidirectional alignment of lyotropic LC conjugated polymers, e.g., DPP-BTz, 75 cyclopentadithiophen-thiadiazolpyridine-based copolymer (PCDTPT-C₁₆), ¹⁰³ and cyclopentadithiophene-benzothiadiazole-based copolymer (CDTBTZ-C₁₆). 103 Schott and Sirringhaus et al. 75 demonstrated that soft blade solution shearing of DPP-BTz resulted in a high degree of in-plane anisotropy and a charge transport anisotropy exceeding 10 at 250 K. In this study, the authors pointed out the importance of the solvent and the printing speed, where they used CB for inducing preaggregation and determined an intermediate printing speed as optimal for alignment (102 μ m s⁻¹ over a range of ~95–292 μ m s⁻¹). The authors inferred that DPP-BTz exhibits a lyotropic LC mesophase from their observation of a large crystalline domain size in films casted from preaggregated CB solutions. Later, our group verified that DPP-BTz exhibits a lyotropic LC phase in both CB and CF solutions as the

concentration increases, discussed later. 94,149 Wu and Richter et al. 103 demonstrated real time anisotropy evolution of bladecoated PCDTPT-C₁₆ and CDTBTZ-C₁₆ films under in situ UV-vis absorption measurements. They observed that the polymer alignment increased at an extremely high solution concentration and suggested a lyotropic LC phase mediated growth. Recently, Persson and DeLongchamp et al. 104 further demonstrated LC-mediated P(NDI2OD-T2) crystallization by employing in situ GIXD combined with UV-vis reflectance during blade coating. In this in situ study, the sharp increase in film anisotropy was observed around 50 s after the meniscus passed, when the solution film was only twice as thick as the final dry film; i.e., when the polymer volume fraction was \geq 0.5. Therefore, polymer alignment ensues at an extremely high solution concentration, suggesting a lyotropic LC phase mediated growth in agreement with the previous study. 103 They further demonstrated that bulk alignment was templated by seed crystals which aligned at an early stage in the drying process. In the resulting P(NDI2OD-T2) films coated at 5 mm s⁻¹, charge carrier mobility of 2.3 cm² V⁻¹ s⁻¹ was obtained with a high charge transport anisotropy of ~15 parallel vs perpendicular to the coating direction. All these studies have showcased the benefits of the lyotropic LC mesophase mediated assembly pathway in terms of increasing the crystalline domain size, inducing in-plane alignment, and thus enhancing device performance of thin films.

Recently, our group found that the relative torsional backbones of the conjugated polymers are conducive to forming chiral twist-bend lyotropic LC phases. 94 Two pairs of twisted D-A polymers (PII-2T and DPP-BTz) and their planar counterparts (thieno-isoindigo-bithiophene-based polymer, PTII-2T and DPP2T-TT) were investigated to study the effect of the molecular conformation on the mesophase and their change across the printing regimes (Figure 12c). We observed the appearance of a lyotropic liquid crystalline mesophase in chloroform solution preceding the dried thin film for torsional PII-2T and DPP-BTz but not for planar PTII-2T and DPP2T-TT. The rope-like texture characteristic of the twist-bend mesophase carried over into the thin film to define a twinned morphology (see Figure 9d). Circular dichroism (CD) spectroscopy validated that the twin domains in the PII-2T and DPP-BTz films printed in the evaporation regime are chiral, corroborating that the polymer assembly pathways are mediated by chiral twist-bend mesophases. In contrast, PTII-2T and DPP2T-TT films did not show substantial CD signals, corresponding to the absence of an intermediate twist-bend mesophase. Twist-bend nematic (N_{TB}) phases have been observed to form from bent-core achiral small molecules or colloidal particles upon assembly into helical aggregates. 150,151 However, twist-bend mesophases have not been observed in achiral polymer systems before, while it had been postulated that polymers with a gross bent structure are likely to exhibit an N_{TB} phase. 152 The exact molecular origin and structure of polymeric twist-bend mesophases remain to be uncovered. We further found this mesophase can be tuned by printing flow enabling efficient charge transport along the polymer chains. Printing flow can alter the polymer assembly pathways by eliminating a chiral, intermediate mesophase upon planarizing the polymer backbone, resulting in drastically enhanced alignment in printed films (see Section 4.1.2 for details).

In most of the current studies, LC mesophases have been exploited for inducing in-plane alignment of conjugated polymers during solution processing. Recently, we discovered

that the formation of the LC mesophase can govern the out-ofplane molecular orientation distribution of conjugated polymers during meniscus-guided coating. 149 In situ GIXD studies have revealed that the lyotropic LC mesophase formed at the front of the meniscus when the critical concentration is reached by solvent evaporation during solution coating of DPP-BTz from chlorobenzene. We observed that the DPP-BTz LC mesophase prefers a face-on orientation in the bulk of the liquid layer and a predominantly edge-on orientation at the top air-liquid interface in the meniscus. Because of surface energy minimization, alkyl chains prefer to stick out of the airliquid interface, leading to edge-on orientation of the mesophase at the top interface. On the other hand, the LC mesophase in the bulk liquid layer that may adopt the twistbend mesophase slowed down crystallization and resulted in a broad and preferential face-on orientation. Upon further solvent evaporation, the LC mesophase transferred its structural characteristics into dried polymer films, preserving the out-of-plane molecular orientation distribution. The LC phase is directional and dynamic and can facilitate rapid molecular reorientation in response to surface properties during the short time scale of printing. For instance, when we expedited crystallization using the dynamic templating approach, the face-on orientation converted to edge-on in the DPP-BTz films.85

Molecular design for promoting lyotropic LC phases provides an opportunity to understand the molecular origin of LC-mediated assembly pathways. Bridges and Segalman et al. 153 demonstrated a solvent effect on the LC phase formation of PCDTPT by engineering alkyl side chains. As the side chain became longer and bulkier, the solubility of the polymers increased in nonpolar solvents that selectively dissolve the side chains (i.e., selective solvents). They described that the increased amphiphilicity allowed the formation of lyotropic liquid crystals consisting of extended polymers chains in selective solvents but not in mutual solvents which solubilize both the backbone and the side chain. B. Kim and J. Kim et al. 105 proposed a molecular design principle to induce a lyotropic mesophase that is conducive to flow-directed alignment during meniscus-guided coating. The idea involved (i) concentration-induced chain planarization by incorporating intramolecular sulfur-fluorine interactions and inhibition of massive preaggregation by integrating (ii) bulky side chains linked to (iii) a tetrahedral carbon (see molecular structures in Figure 12d). The thus designed conjugated polymer was aligned by optimizing the polymer concentration and printing speed, resulting in a high emission dichroic ratio of 16.67 in photoluminescence and more than 3 orders of magnitude higher anisotropic hole mobility along the aligned chains. In their following study, 154 the design rule included additional factors such as the effect of the main chain planarity, the role of the branching point of side chains and alternative concentration-induced planarization units, and the role of the surface energy of conjugated polymers. In particular, they demonstrated that bulky side chains on the tetrahedral carbon linker are a prerequisite to induce a lyotropic LC phase (Figure 12d). NCP1 satisfied the three primary design requirements, clearly showing a lyotropic LC phase at high concentrations; the LC phase mediated assembly pathway led to aligned thin films with a dichroic ratio of 4.67 prepared by blade coating. In contrast, NCP2 without the tetrahedral carbon linker did not show lyotropic LC phase formation, resulting in a low degree of alignment of NCP2 under a shear flow (dichroic ratio of ~1.5). NCP3 followed the three design principles and exhibited a lyotropic LC phase but showed a low dichroic ratio of ~ 1.5 . This was explained by the relatively large thienyl-phenyl dihedral angle (25.8°) that restricts chain planarization. From this result, we could infer that not all LC phases are conducive to flow-directed alignment during printing; the polymer conformation and the LC structure need to be taken into account. On the other hand, it remains unclear whether these specific design principles can be generalized to other systems. For instance, we did observe a lyotropic LC mesophase for PII-2T with bulky side chains linked to the nontetrahedral carbon (see the molecular structure in Figure 12c). Regardless of the details of side chain design, side chain bulkiness remains a critical factor for inducing lyotropic mesophases through preventing strong intermolecular π - π interactions and thus direct crystallization from solution.

5. CONCLUSIONS AND OUTLOOK

In this perspective, we summarized important fundamentals of polymer crystallization/assembly and coating/printing techniques. We also discussed key processing strategies to control morphology at multiple length scales: (i) engineering printing flow and optimizing printing regime, (ii) designing substrate properties, and (iii) tuning assembly pathways via preaggregation or liquid-crystalline mesophase. Multiscale morphologies of conjugated polymers involve intramolecular conformation and intermolecular packing, mesoscale domain size, orientation and connectivity, and macroscale alignment and (para)crystallinity. Tuning intramolecular conformation is particularly important because its defining features such as planarity, torsion angle, chain folding, etc. directly govern intrachain charge transport and crucially impact the hierarchical morphology. Fluid flow during solution processing can profoundly impact molecular conformation and therefore offers an opportunity to largely modulate multiscale morphology and charge transport. Recent works have indeed showed that printing flow in an intermediate printing regime can planarize the conjugated polymer backbone, alter the assembly pathway or extent of aggregation, align the polymer thin film, and thus enhance the charge carrier mobility and charge transport anisotropy. On the other hand, many fundamental aspects of how various flow types impact flow-directed aggregation and alter the assembly pathways of conjugated polymers remain to be explored. It is still unclear whether the design rules established for flow-induced crystallization of flexible polymers can be applied to more rigid and architecturally complex conjugated polymers. Answering these questions may require precisely defined flow field and in situ approaches to track flow-directed conformation change and assembly.

Besides tuning fluid flow, surface modification has long been an effective approach to control the assembly of conjugated polymers. We pointed the readers to a recently developed free energy model that can guide the choice of substrates with appropriate surface energy to lower the nucleation barrier and enhance crystallinity and alignment of polymer thin films. We also highlighted a new approach employing dynamic, liquid-like surfaces as the printing substrates; the dynamic nature of the substrate facilitates cooperative multivalent binding with the assembling polymer as to speed up crystallization to better match with the time scale of printing. Such approaches have been successful in significantly elevating the degree of

crystallinity and alignment; on the other hand, controlling various conformational features still seems out of reach through surface modification. Looking forward, the surface modification approach could be used in conjunction with flow-directed assembly to control all aspects of morphology from conformation and packing to orientation and alignment. On the other hand, it remains a holy grail to print single crystal arrays of conjugated polymers. ^{155,156} Drastically expediting the crystallization kinetics through the aforementioned strategies, when combined with nucleation control (e.g., through nanoconfinement 157), may offer new opportunities to printing conjugated polymer single crystals. On the fundamental side, it is yet to be elucidated how various morphology control strategies may impact the assembly pathways of conjugated polymers.

Recently, tuning preaggregation and liquid-crystal mediated assembly pathways has been gaining much attention thanks in part to the rapid development of high-performance donoracceptor conjugated polymers; owing to their relatively rigid conformation and strong/amphiphilic intermolecular interactions, such polymers readily form preaggregates and/or liquid crystalline phases even at low solution concentrations. Inducing polymer preaggregation by lowering solvent quality and designing molecular structures to induce the lyotropic liquid crystal phase have been used as strategies to improve film crystallinity and alignment during solution processing. On the other hand, the ultimate film morphology is defined by the specific structure of the preaggregates or liquid crystals of conjugated polymers which is often overlooked. Further, how processing-imposed nonequilibrium conditions impact preaggregation and liquid-crystal mediated assembly pathways are rarely investigated. Moreover, the relationship between preaggregation and LC phase formation remains unclear.

While this perspective focuses on directed assembly and processing of conjugated polymers for controlled electron/hole transport, we envision that these insights and strategies are transferrable to emerging areas such as organic mixed ionic–electronic conductors, ^{158,159} photonics, ¹⁶⁰ liquid crystalline elastomers, ¹⁶¹ block copolymers, ¹⁶² 3D/4D printed soft matters, 163,164 etc. For instance, we recently exploited the interplay between processing and assembly to modulate the structural color of bottle-brush block copolymers. 165 We achieved this by developing a direct-write 3D printing approach that dynamically modulates the lamella layer spacing of bottlebrush block copolymers by kinetically trapping metastable structures during assembly. We believe that interfacing polymer assembly with additive manufacturing will continue to be a fertile ground for fundamental studies on nonequilibrium assembly of structurally complex functional polymers and for engendering innovative solutions to enhance properties or even to impart new properties not possible before.

AUTHOR INFORMATION

Corresponding Author

Ying Diao — Department of Chemical and Biomolecular Engineering, Department of Materials Science and Engineering, and Beckman Institute, University of Illinois at Urbana—Champaign, Urbana, Illinois 61801, United States; orcid.org/0000-0002-8984-0051; Email: yingdiao@illinois.edu

Authors

Kyung Sun Park – Department of Chemical and Biomolecular Engineering, University of Illinois at Urbana–Champaign, Urbana, Illinois 61801, United States

Justin J. Kwok – Department of Materials Science and Engineering, University of Illinois at Urbana–Champaign, Urbana, Illinois 61801, United States

Prapti Kafle – Department of Chemical and Biomolecular Engineering, University of Illinois at Urbana–Champaign, Urbana, Illinois 61801, United States

Complete contact information is available at: https://pubs.acs.org/10.1021/acs.chemmater.0c04152

Author Contributions

 $^{\parallel}$ (K.S.P., J.J.K., and P.K.) These authors contributed equally.

Notes

The authors declare no competing financial interest.

Biographies

Kyung Sun Park is a Shen Postdoctoral Scholar in Chemical and Biomolecular Engineering at the University of Illinois at Urbana—Champaign. She received a Ph.D. in Chemistry from Hanyang University in 2015, followed by a two-year postdoctoral fellow at the same school. During those years, she worked on developing solution printing approaches for single crystalline organic semiconductors. In the Diao group, she has been working on understanding morphological transitions of conjugated polymers through studying molecular assembly pathways.

Justin Kwok is a Ph.D. candidate in the Materials Science and Engineering Department at the University of Illinois at Urbana—Champaign in the group of Prof. Ying Diao. He received his B.S. in Chemical Engineering from the University of Southern California in 2014. His current research focuses on understanding the conformation and assembly of conjugated polymers in solution as well as during the solution printing process. He is an awardee of the DOE SCGSR Program.

Prapti Kafle is a Ph.D. candidate in the Chemical and Biomolecular Engineering Department at the University of Illinois at Urbana—Champaign under the supervision of Prof. Ying Diao. She received her B.A. degree in Chemistry and Mathematics from Connecticut College in 2016. Her research focuses on utilization of solution printing methods to crystallize low-dimensional thin films of conjugated polymers and pharmaceuticals to improve their functional properties. She is a recipient of the AAUW International Fellowship.

Ying Diao is an Assistant Professor at the University of Illinois at Urbana—Champaign. She received a Ph.D. from MIT in 2012 and pursued postdoctoral training at Stanford until 2014. Her current work focuses on understanding the assembly of organic functional materials and innovating printing technologies that enable structural control down to the molecular and nanoscale. She received the MIT TR35 award, NSF CAREER Award, Sloan Research Fellowship, 3M Non-Tenured Faculty Award, and NASA Early Career Faculty Award.

ACKNOWLEDGMENTS

K.S.P. and Y.D. acknowledge ONR support under Grant No. N00014-19-1-2146, and K.S.P. acknowledges partial support from the Shen Postdoctoral Fellowship. J.J.K. and Y.D. acknowledge support by the NSF CAREER award under Grant No. 18-47828. J.J.K. also acknowledges partial support from the U.S. Department of Energy, Office of Science, Office of Workforce Development for Teachers and Scientists, Office of Science Graduate Student Research (SCGSR) program. The

SCGSR program is administered by the Oak Ridge Institute for Science and Education for the DOE under Contract Number DE-SC0014664. P.K. acknowledges partial support by the NSF MRSEC: Illinois Materials Research Center under Grant Number DMR 17-20633, the 3M Corporate Fellowship, and the Harry G. Drickamer Graduate Research Fellowship.

REFERENCES

- (1) Shirakawa, H.; Louis, E. J.; Macdiarmid, A. G.; Chiang, C. K.; Heeger, A. J. Synthesis of Electrically Conducting Organic Polymers Halogen Derivatives of Polyacetylene, (Ch)X. J. Chem. Soc., Chem. Commun. 1977, No. 16, 578–580.
- (2) Rogers, J. A.; Bao, Z. N.; Makhija, A.; Braun, P. Printing process suitable for reel-to-reel production of high-performance organic transistors and circuits. *Adv. Mater.* **1999**, *11* (9), 741–745.
- (3) Forrest, S. R. The path to ubiquitous and low-cost organic electronic appliances on plastic. *Nature* **2004**, 428 (6986), 911–918.
- (4) Kaltenbrunner, M.; Sekitani, T.; Reeder, J.; Yokota, T.; Kuribara, K.; Tokuhara, T.; Drack, M.; Schwodiauer, R.; Graz, I.; Bauer-Gogonea, S.; Bauer, S.; Someya, T. An ultra-lightweight design for imperceptible plastic electronics. *Nature* **2013**, 499 (7459), 458–463.
- (5) Brütting, W. Introduction to the Physics of Organic Semiconductors. In *Physics of Organic Semiconductors*; Brütting, W., Ed.; Wiley-VCH Verlag GmbH & Co. KGaA: Weinheim, 2005; pp 1–14.
- (6) Horowitz, G. Charge Transport in Oligomers. In *Organic Field-Effect Transistors*; Bao, Z. N., Locklin, J., Eds.; CRC Press: Boca Raton, FL, 2007; Vol. 128, pp 73–101.
- (7) Illig, S.; Eggeman, A. S.; Troisi, A.; Jiang, L.; Warwick, C.; Nikolka, M.; Schweicher, G.; Yeates, S. G.; Geerts, Y. H.; Anthony, J. E.; Sirringhaus, H. Reducing dynamic disorder in small-molecule organic semiconductors by suppressing large-amplitude thermal motions. *Nat. Commun.* **2016**, *7*, 10736.
- (8) Ishii, H.; Kobayashi, N.; Hirose, K. Carrier transport calculations of organic semiconductors with static and dynamic disorder. *Jpn. J. Appl. Phys.* **2019**, 58 (11), 110501.
- (9) Podzorov, V. Charge Carrier Transport in Single-Crystal Organic Field-Effect Transistors. In *Organic Field-Effect Transistors*; Bao, Z. N., Locklin, J., Eds.; CRC Press: Boca Raton, FL, 2007; Vol. 128, pp 27–72
- (10) Gu, K. C.; Loo, Y. L. The Polymer Physics of Multiscale Charge Transport in Conjugated Systems. *J. Polym. Sci., Part B: Polym. Phys.* **2019**, *57* (23), 1559–1571.
- (11) Salleo, A. Charge transport in polymeric transistors. *Mater. Today* **2007**, *10* (3), 38–45.
- (12) Noriega, R.; Salleo, A.; Spakowitz, A. J. Chain conformations dictate multiscale charge transport phenomena in disordered semiconducting polymers. *Proc. Natl. Acad. Sci. U. S. A.* **2013**, *110* (41), 16315–16320.
- (13) Venkateshvaran, D.; Nikolka, M.; Sadhanala, A.; Lemaur, V.; Zelazny, M.; Kepa, M.; Hurhangee, M.; Kronemeijer, A. J.; Pecunia, V.; Nasrallah, I.; Romanov, I.; Broch, K.; McCulloch, I.; Emin, D.; Olivier, Y.; Cornil, J.; Beljonne, D.; Sirringhaus, H. Approaching disorder-free transport in high-mobility conjugated polymers. *Nature* **2014**, *515* (7527), 384–388.
- (14) Westenhoff, S.; Beenken, W. J. D.; Yartsev, A.; Greenham, N. C. Conformational disorder of conjugated polymers. *J. Chem. Phys.* **2006**, *125* (15), 154903.
- (15) Lee, J.; Chung, J. W.; Kim, D. H.; Lee, B. L.; Park, I. I.; Lee, S.; Hausermann, R.; Batlogg, B.; Lee, S. S.; Choi, I.; Kim, I. W.; Kang, M. S. Thin Films of Highly Planar Semiconductor Polymers Exhibiting Band-like Transport at Room Temperature. *J. Am. Chem. Soc.* **2015**, 137 (25), 7990–7993.
- (16) Senanayak, S. P.; Ashar, A. Z.; Kanimozhi, C.; Patil, S.; Narayan, K. S. Room-temperature bandlike transport and Hall effect in a high-mobility ambipolar polymer. *Phys. Rev. B: Condens. Matter Mater. Phys.* **2015**, *91* (11), 115302.
- (17) Yamashita, Y.; Hinkel, F.; Marszalek, T.; Zajaczkowski, W.; Pisula, W.; Baumgarten, M.; Matsui, H.; Mullen, K.; Takeya, J.

- Mobility Exceeding 10 cm(2)/(V center dot s) in Donor-Acceptor Polymer Transistors with Band-like Charge Transport. *Chem. Mater.* **2016**, 28 (2), 420–424.
- (18) Yamashita, Y.; Tsurumi, J.; Hinkel, F.; Okada, Y.; Soeda, J.; Zajaczkowski, W.; Baumgarten, M.; Pisula, W.; Matsui, H.; Mullen, K.; Takeya, J. Transition Between Band and Hopping Transport in Polymer Field-Effect Transistors. *Adv. Mater.* **2014**, *26* (48), 8169–8173
- (19) Khim, D.; Luzio, A.; Bonacchini, G. E.; Pace, G.; Lee, M. J.; Noh, Y. Y.; Caironi, M. Uniaxial Alignment of Conjugated Polymer Films for High-Performance Organic Field-Effect Transistors. *Adv. Mater.* **2018**, *30* (20), 1705463.
- (20) Noriega, R.; Rivnay, J.; Vandewal, K.; Koch, F. P. V.; Stingelin, N.; Smith, P.; Toney, M. F.; Salleo, A. A general relationship between disorder, aggregation and charge transport in conjugated polymers. *Nat. Mater.* **2013**, *12* (11), 1038–1044.
- (21) Mollinger, S. A.; Salleo, A.; Spakowitz, A. J. Anomalous Charge Transport in Conjugated Polymers Reveals Underlying Mechanisms of Trapping and Percolation. *ACS Cent. Sci.* **2016**, 2 (12), 910–915.
- (22) Gu, K. C.; Snyder, C. R.; Onorato, J.; Luscombe, C. K.; Bosse, A. W.; Loo, Y. L. Assessing the Huang-Brown Description of Tie Chains for Charge Transport in Conjugated Polymers. *ACS Macro Lett.* **2018**, 7 (11), 1333–1338.
- (23) Huang, Y. L.; Brown, N. The Effect of Molecular-Weight on Slow Crack-Growth in Linear Polyethylene Homopolymers. *J. Mater. Sci.* 1988, 23 (10), 3648–3655.
- (24) Huang, Y. L.; Brown, N. Dependence of Slow Crack-Growth in Polyethylene on Butyl Branch Density Morphology and Theory. *J. Polym. Sci., Part B: Polym. Phys.* **1991**, 29 (1), 129–137.
- (25) Noriega, R. Efficient Charge Transport in Disordered Conjugated Polymer. *Macromol. Rapid Commun.* **2018**, 39 (14), 1800096.
- (26) Storks, K. H. An electron diffraction examination of some linear high polymers. *J. Am. Chem. Soc.* **1938**, *60*, 1753–1761.
- (27) Keller, A. A Note on Single Crystals in Polymers Evidence for a Folded Chain Configuration. *Philos. Mag.* **1957**, 2 (21), 1171–1175.
- (28) Flory, P. J. On the Morphology of the Crystalline State in Polymers. J. Am. Chem. Soc. 1962, 84 (15), 2857–2867.
- (29) Lauritzen, J. I.; Hoffman, J. D. Theory of Formation of Polymer Crystals with Folded Chains in Dilute Solution. *J. Res. Natl. Bur. Stand., Sect. A* **1960**, *64* (1), 73–102.
- (30) Zhang, M. C.; Guo, B. H.; Xu, J. A Review on Polymer Crystallization Theories. *Crystals* **2017**, *7* (1), 4.
- (31) Heeger, A. J. Semiconducting polymers: the Third Generation. *Chem. Soc. Rev.* **2010**, 39 (7), 2354–2371.
- (32) Kim, J. S.; McHugh, S. K.; Swager, T. M. Nanoscale fibrils and grids: Aggregated structures from rigid-rod conjugated polymers. *Macromolecules* **1999**, 32 (5), 1500–1507.
- (33) Samori, P.; Francke, V.; Mullen, K.; Rabe, J. P. Self-assembly of a conjugated polymer: from molecular rods to a nanoribbon architecture with molecular dimensions. *Chem. Eur. J.* **1999**, *5* (8), 2312–2317.
- (34) Hennebicq, E.; Pourtois, G.; Scholes, G. D.; Herz, L. M.; Russell, D. M.; Silva, C.; Setayesh, S.; Grimsdale, A. C.; Mullen, K.; Bredas, J. L.; Beljonne, D. Exciton migration in rigid-rod conjugated polymers: An improved Forster model. *J. Am. Chem. Soc.* **2005**, *127* (13), 4744–4762.
- (35) Bunz, U. H. F. Poly(aryleneethynylene)s: Syntheses, properties, structures, and applications. *Chem. Rev.* **2000**, *100* (4), 1605–1644.
- (36) Hu, X. D.; Jenkins, S. E.; Min, B. G.; Polk, M. B.; Kumar, S. Rigid-rod polymers: Synthesis, processing, simulation, structure, and properties. *Macromol. Mater. Eng.* **2003**, 288 (11), 823–843.
- (37) Vanhee, S.; Rulkens, R.; Lehmann, U.; Rosenauer, C.; Schulze, M.; Kohler, W.; Wegner, G. Synthesis and characterization of rigid rod poly(p-phenylenes). *Macromolecules* **1996**, *29* (15), 5136–5142.
- (38) Kuei, B.; Gomez, E. D. Chain conformations and phase behavior of conjugated polymers. *Soft Matter* **2017**, *13* (1), 49–67.
- (39) Lee, J.; Kalin, A. J.; Yuan, T. Y.; Al-Hashimi, M.; Fang, L. Fully conjugated ladder polymers. *Chem. Sci.* **2017**, *8* (4), 2503–2521.

- (40) Brinkmann, M. Structure and Morphology Control in Thin Films of Regioregular Poly(3-hexylthiophene). J. Polym. Sci., Part B: Polym. Phys. **2011**, 49 (17), 1218–1233.
- (41) Chivers, R. A.; Barham, P. J.; Martinezsalazar, J.; Keller, A. A new Look at the Crystallization of Polyethylene. II. Crystallization from the Melt at Low Supercoolings. *J. Polym. Sci., Polym. Phys. Ed.* **1982**, 20 (9), 1717–1732.
- (42) Kline, R. J.; McGehee, M. D.; Kadnikova, E. N.; Liu, J. S.; Frechet, J. M. J.; Toney, M. F. Dependence of regioregular poly(3-hexylthiophene) film morphology and field-effect mobility on molecular weight. *Macromolecules* **2005**, *38* (8), 3312–3319.
- (43) Cotts, P. M.; Swager, T. M.; Zhou, Q. Equilibrium flexibility of a rigid linear conjugated polymer. *Macromolecules* **1996**, 29 (23), 7323–7328.
- (44) Mena-Osteritz, E.; Meyer, A.; Langeveld-Voss, B. M. W.; Janssen, R. A. J.; Meijer, E. W.; Bauerle, P. Two-dimensional crystals of poly(3-alkylthiophene)s: Direct visualization of polymer folds in submolecular resolution. *Angew. Chem., Int. Ed.* **2000**, 39 (15), 2679–2684
- (45) Miura, T.; Kishi, R.; Mikami, M.; Tanabe, Y. Effect of rigidity on the crystallization processes of short polymer melts. *Phys. Rev. E: Stat. Phys., Plasmas, Fluids, Relat. Interdiscip. Top.* **2001**, 63 (6), 061807.
- (46) Yokota, H.; Kawakatsu, T. Nucleation theory of polymer crystallization with conformation entropy. *Polymer* **2020**, *186*, 121975.
- (47) Mei, J. G.; Bao, Z. N. Side Chain Engineering in Solution-Processable Conjugated Polymers. *Chem. Mater.* **2014**, *26* (1), 604–615.
- (48) Gadisa, A.; Oosterbaan, W. D.; Vandewal, K.; Bolsee, J. C.; Bertho, S.; D'Haen, J.; Lutsen, L.; Vanderzande, D.; Manca, J. V. Effect of Alkyl Side-Chain Length on Photovoltaic Properties of Poly(3-alkylthiophene)/PCBM Bulk Heterojunctions. *Adv. Funct. Mater.* **2009**, *19* (20), 3300–3306.
- (49) Zhang, Z. G.; Min, J.; Zhang, S. Y.; Zhang, J.; Zhang, M. J.; Li, Y. F. Alkyl chain engineering on a dithieno[3,2-b:2 ',3 '-d]silole-alt-dithienylthiazolo[5,4-d]thiazole copolymer toward high performance bulk heterojunction solar cells. *Chem. Commun.* **2011**, 47 (33), 9474–9476.
- (50) Panzer, F.; Bassler, H.; Köhler, A. Temperature Induced Order-Disorder Transition in Solutions of Conjugated Polymers Probed by Optical Spectroscopy. *J. Phys. Chem. Lett.* **2017**, *8* (1), 114–125.
- (51) Kline, R. J.; DeLongchamp, D. M.; Fischer, D. A.; Lin, E. K.; Richter, L. J.; Chabinyc, M. L.; Toney, M. F.; Heeney, M.; McCulloch, I. Critical role of side-chain attachment density on the order and device performance of polythiophenes. *Macromolecules* **2007**, 40 (22), 7960–7965.
- (52) Carpenter, J. H.; Ghasemi, M.; Gann, E.; Angunawela, I.; Stuard, S. J.; Rech, J. J.; Ritchie, E.; O'Connor, B. T.; Atkin, J.; You, W.; DeLongchamp, D. M.; Ade, H. Competition between Exceptionally Long-Range Alkyl Sidechain Ordering and Backbone Ordering in Semiconducting Polymers and Its Impact on Electronic and Optoelectronic Properties. *Adv. Funct. Mater.* 2019, 29 (5), 1806977.
- (53) Zhang, Z. G.; Li, Y. F. Side-chain engineering of high-efficiency conjugated polymer photovoltaic materials. *Sci. China: Chem.* **2015**, 58 (2), 192–209.
- (54) Pennings, A. J.; Kiel, A. M. Fractionation of Polymers by Crystallization from Solution 0.3. On Morphology of Fibrillar Polyethylene Crystals Grown in Solution. *Colloid Polym. Sci.* **1965**, 205 (2), 160–162.
- (55) Keller, A.; Kolnaar, H. W. H. Flow-Induced Orientation and Structure Formation. *Materials science and technology* **2006**, 195–198. (56) Lamberti, G. Flow induced crystallisation of polymers. *Chem.*
- Soc. Rev. 2014, 43 (7), 2240–2252.
- (57) Smith, D. E.; Babcock, H. P.; Chu, S. Single-polymer dynamics in steady shear flow. *Science* **1999**, 283 (5408), 1724–1727.
- (58) Reiter, G. Some unique features of polymer crystallisation. *Chem. Soc. Rev.* **2014**, 43 (7), 2055–2065.

- (59) Hagerman, P. J.; Zimm, B. H. Monte-Carlo Approach to the Analysis of the Rotational Diffusion of Wormlike Chains. *Biopolymers* **1981**, 20 (7), 1481–1502.
- (60) Shaw, L.; Hayoz, P.; Diao, Y.; Reinspach, J. A.; To, J. W. F.; Toney, M. F.; Weitz, R. T.; Bao, Z. N. Direct Uniaxial Alignment of a Donor-Acceptor Semiconducting Polymer Using Single-Step Solution Shearing. *ACS Appl. Mater. Interfaces* **2016**, *8* (14), 9285–9296.
- (61) Wang, G.; Huang, W.; Eastham, N. D.; Fabiano, S.; Manley, E. F.; Zeng, L.; Wang, B. H.; Zhang, X. A.; Chen, Z. H.; Li, R.; Chang, R. P. H.; Chen, L. X.; Bedzyk, M. J.; Melkonyan, F. S.; Facchetti, A.; Marks, T. J. Aggregation control in natural brush-printed conjugated polymer films and implications for enhancing charge transport. *Proc. Natl. Acad. Sci. U. S. A.* 2017, 114 (47), E10066—E10073.
- (62) Qu, G.; Kwok, J. J.; Diao, Y. Flow-Directed Crystallization for Printed Electronics. Acc. Chem. Res. 2016, 49 (12), 2756–2764.
- (63) Patel, B. B.; Diao, Y. Multiscale assembly of solution-processed organic electronics: the critical roles of confinement, fluid flow, and interfaces. *Nanotechnology* **2018**, *29* (4), 044004.
- (64) Krebs, F. C. Fabrication and processing of polymer solar cells: A review of printing and coating techniques. *Sol. Energy Mater. Sol. Cells* **2009**, 93 (4), 394–412.
- (65) Khan, S.; Lorenzelli, L.; Dahiya, R. S. Technologies for Printing Sensors and Electronics Over Large Flexible Substrates: A Review. *IEEE Sens. J.* **2015**, *15* (6), 3164–3185.
- (66) Wu, W. Inorganic nanomaterials for printed electronics: a review. *Nanoscale* **2017**, *9* (22), 7342–7372.
- (67) Fukuda, K.; Someya, T. Recent Progress in the Development of Printed Thin-Film Transistors and Circuits with High-Resolution Printing Technology. *Adv. Mater.* **2017**, *29* (25), 1602736.
- (68) Kim, G. W.; Kwon, E. H.; Kim, M.; Park, Y. D. Uniform and Reliable Dip-Coated Conjugated Polymers for Organic Transistors as Obtained by Solvent Vapor Annealing. *J. Phys. Chem. C* **2019**, *123* (37), 23255–23263.
- (69) Li, M. M.; Mangalore, D. K.; Zhao, J. B.; Carpenter, J. H.; Yan, H. P.; Ade, H.; Yan, H.; Mullen, K.; Blom, P. W. M.; Pisula, W.; de Leeuw, D. M.; Asadi, K. Integrated circuits based on conjugated polymer monolayer. *Nat. Commun.* **2018**, *9*, 451.
- (70) Bucella, S. G.; Luzio, A.; Gann, E.; Thomsen, L.; McNeill, C. R.; Pace, G.; Perinot, A.; Chen, Z. H.; Facchetti, A.; Caironi, M. Macroscopic and high-throughput printing of aligned nanostructured polymer semiconductors for MHz large-area electronics. *Nat. Commun.* **2015**, *6*, 8394.
- (71) Shaw, L.; Yan, H. P.; Gu, X. D.; Hayoz, P.; Weitz, R. T.; Kaelblein, D.; Toney, M. F.; Bao, Z. N. Microstructural Evolution of the Thin Films of a Donor-Acceptor Semiconducting Polymer Deposited by Meniscus-Guided Coating. *Macromolecules* **2018**, *51* (11), 4325–4340.
- (72) Xu, J.; Wu, H. C.; Zhu, C. X.; Ehrlich, A.; Shaw, L.; Nikolka, M.; Wang, S. H.; Molina-Lopez, F.; Gu, X. D.; Luo, S. C.; Zhou, D. S.; Kim, Y. H.; Wang, G. J. N.; Gu, K.; Feig, V. R.; Chen, S. C.; Kim, Y.; Katsumata, T.; Zheng, Y. Q.; Yan, H.; Chung, J. W.; Lopez, J.; Murmann, B.; Bao, Z. A. Multi-scale ordering in highly stretchable polymer semiconducting films. *Nat. Mater.* 2019, *18* (6), 594–601.
- (73) Diao, Y.; Zhou, Y.; Kurosawa, T.; Shaw, L.; Wang, C.; Park, S.; Guo, Y. K.; Reinspach, J. A.; Gu, K.; Gu, X. D.; Tee, B. C. K.; Pang, C. H.; Yan, H. P.; Zhao, D. H.; Toney, M. F.; Mannsfeld, S. C. B.; Bao, Z. A. Flow-enhanced solution printing of all-polymer solar cells. *Nat. Commun.* **2015**, *6*, 7955.
- (74) Wang, G.; Chu, P. H.; Fu, B. Y.; He, Z. Y.; Kleinhenz, N.; Yuan, Z. B.; Mao, Y. M.; Wang, H. Z.; Reichmanis, E. Conjugated Polymer Alignment: Synergisms Derived from Microfluidic Shear Design and UV Irradiation. ACS Appl. Mater. Interfaces 2016, 8 (37), 24761–24772.
- (75) Schott, S.; Gann, E.; Thomsen, L.; Jung, S. H.; Lee, J. K.; McNeill, C. R.; Sirringhaus, H. Charge-Transport Anisotropy in a Uniaxially Aligned Diketopyrrolopyrrole-Based Copolymer. *Adv. Mater.* **2015**, 27 (45), 7356–7364.
- (76) Molina-Lopez, F.; Wu, H. C.; Wang, G. J. N.; Yan, H. P.; Shaw, L.; Xu, J.; Toney, M. F.; Bao, Z. N. Enhancing Molecular Alignment

- and Charge Transport of Solution-Sheared Semiconducting Polymer Films by the Electrical-Blade Effect. *Adv. Electron Mater.* **2018**, *4* (7), 1800110.
- (77) Teixeira da Rocha, C.; Qu, G.; Yang, X.; Shivhare, R.; Hambsch, M.; Diao, Y.; Mannsfeld, S. C. B. Mitigating Meniscus Instabilities in Solution-Sheared Polymer Films for Organic Field-Effect Transistors. ACS Appl. Mater. Interfaces 2019, 11 (33), 30079–30088.
- (78) Zhu, L.; Zhong, W. K.; Qiu, C. Q.; Lyu, B. S.; Zhou, Z. C.; Zhang, M.; Song, J. N.; Xu, J. Q.; Wang, J.; Ali, J.; Feng, W.; Shi, Z. W.; Gu, X. D.; Ying, L.; Zhang, Y. M.; Liu, F. Aggregation-Induced Multilength Scaled Morphology Enabling 11.76% Efficiency in All-Polymer Solar Cells Using Printing Fabrication. *Adv. Mater.* **2019**, *31* (41), 1902899.
- (79) C, A.; Colella, M.; Griffin, J.; Kingsley, J.; Scarratt, N.; Luszczynska, B.; Ulanski, J. Slot-Die Coating of Double Polymer Layers for the Fabrication of Organic Light Emitting Diodes. *Micromachines-Basel* **2019**, *10* (1), 53.
- (80) Schuettfort, T.; Watts, B.; Thomsen, L.; Lee, M.; Sirringhaus, H.; McNeill, C. R. Microstructure of Polycrystalline PBTTT Films: Domain Mapping and Structure Formation. *ACS Nano* **2012**, *6* (2), 1849–1864.
- (81) Kang, B.; Min, H.; Seo, U.; Lee, J.; Park, N.; Cho, K.; Lee, H. S. Directly Drawn Organic Transistors by Capillary Pen: A New Facile Patterning Method using Capillary Action for Soluble Organic Materials. *Adv. Mater.* **2013**, *25* (30), 4117–4122.
- (82) Li, Z. D.; Liu, H.; Ouyang, C.; Wee, W. H.; Cui, X. Y.; Lu, T. J.; Pingguan-Murphy, B.; Li, F.; Xu, F. Recent Advances in Pen-Based Writing Electronics and their Emerging Applications. *Adv. Funct. Mater.* **2016**, *26* (2), 165–180.
- (83) Runser, R.; Root, S. E.; Ober, D. E.; Choudhary, K.; Chen, A. X.; Dhong, C.; Urbina, A. D.; Lipomi, D. J. Interfacial Drawing: Roll-to-Roll Coating of Semiconducting Polymer and Barrier Films onto Plastic Foils and Textiles. *Chem. Mater.* **2019**, *31* (21), 9078–9086.
- (84) Mohammadi, E.; Zhao, C. K.; Meng, Y. F.; Qu, G.; Zhang, F. J.; Zhao, X. K.; Mei, J. G.; Zuo, J. M.; Shukla, D.; Diao, Y. Dynamic-template-directed multiscale assembly for large-area coating of highly-aligned conjugated polymer thin films. *Nat. Commun.* **2017**, *8*, 16070.
- (85) Mohammadi, E.; Zhao, C. K.; Zhang, F. J.; Qu, G.; Jung, S. H.; Zhao, Q. J.; Evans, C. M.; Lee, J. K.; Shukla, D.; Diao, Y. Ion Gel Dynamic Templates for Large Modulation of Morphology and Charge Transport Properties of Solution-Coated Conjugated Polymer Thin Films. ACS Appl. Mater. Interfaces 2019, 11 (25), 22561–22574.
- (86) Mohammadi, E.; Qu, G.; Kafle, P.; Jung, S. H.; Lee, J. K.; Diao, Y. Design rules for dynamic-template-directed crystallization of conjugated polymers. *Mol. Syst. Des Eng.* **2020**, 5 (1), 125–138.
- (87) Mohammadi, E.; Kafle, P.; Huang, K. Y.; Zhu, W. K.; Huang, J.; Jung, S. H.; Lee, J. K.; Evans, C. M.; Diao, Y. Role of Multivalent Interactions in Dynamic-Template-Directed Assembly of Conjugated Polymers. ACS Appl. Mater. Interfaces 2020, 12 (2), 2753–2762.
- (88) Diao, Y.; Shaw, L.; Bao, Z. A.; Mannsfeld, S. C. B. Morphology control strategies for solution-processed organic semiconductor thin films. *Energy Environ. Sci.* **2014**, *7* (7), 2145–2159.
- (89) Deegan, R. D.; Bakajin, O.; Dupont, T. F.; Huber, G.; Nagel, S. R.; Witten, T. A. Capillary flow as the cause of ring stains from dried liquid drops. *Nature* **1997**, 389 (6653), 827–829.
- (90) Hu, H.; Larson, R. G. Evaporation of a sessile droplet on a substrate. J. Phys. Chem. B 2002, 106 (6), 1334–1344.
- (91) Hu, H.; Larson, R. G. Analysis of the effects of Marangoni stresses on the microflow in an evaporating sessile droplet. *Langmuir* **2005**, 21 (9), 3972–3980.
- (92) Le Berre, M.; Chen, Y.; Baigl, D. From Convective Assembly to Landau-Levich Deposition of Multilayered Phospholipid Films of Controlled Thickness. *Langmuir* **2009**, *25* (5), 2554–2557.
- (93) Doumenc, F.; Guerrier, B. Drying of a Solution in a Meniscus: A Model Coupling the Liquid and the Gas Phases. *Langmuir* **2010**, *26* (17), 13959–13967.
- (94) Park, K. S.; Kwok, J. J.; Dilmurat, R.; Qu, G.; Kafle, P.; Luo, X. Y.; Jung, S. H.; Olivier, Y.; Lee, J. K.; Mei, J. G.; Beljonne, D.; Diao, Y.

- Tuning conformation, assembly, and charge transport properties of conjugated polymers by printing flow. *Sci. Adv.* **2019**, *5* (8), eaaw7757.
- (95) Janneck, R.; Vercesi, F.; Heremans, P.; Genoe, J.; Rolin, C. Predictive Model for the Meniscus-Guided Coating of High-Quality Organic Single-Crystalline Thin Films. *Adv. Mater.* **2016**, 28 (36), 8007–8013.
- (96) Qu, G.; Kwok, J. J.; Mohammadi, E.; Zhang, F. J.; Diao, Y. Understanding Film-To-Stripe Transition of Conjugated Polymers Driven by Meniscus Instability. ACS Appl. Mater. Interfaces 2018, 10 (47), 40692–40701.
- (97) Yabu, H.; Shimomura, M. Preparation of self-organized mesoscale polymer patterns on a solid substrate: Continuous pattern formation from a receding meniscus. *Adv. Funct. Mater.* **2005**, *15* (4), 575–581.
- (98) Deblais, A.; Harich, R.; Colin, A.; Kellay, H. Taming contact line instability for pattern formation. *Nat. Commun.* **2016**, *7*, 12458.
- (99) Liu, Y. J.; Lee, D. Y.; Monteux, C.; Crosby, A. J. Hyperbranched Polymer Structures via Flexible Blade Flow Coating. *J. Polym. Sci., Part B: Polym. Phys.* **2016**, *54* (1), 32–37.
- (100) Wie, J. J.; Nguyen, N. A.; Cwalina, C. D.; Liu, J. L.; Martin, D. C.; Mackay, M. E. Shear-Induced Solution Crystallization of Poly(3-hexylthiophene) (P3HT). *Macromolecules* **2014**, 47 (10), 3343–3349.
- (101) Wang, G.; Persson, N.; Chu, P. H.; Kleinhenz, N.; Fu, B. Y.; Chang, M.; Deb, N.; Mao, Y. M.; Wang, H. Z.; Grover, M. A.; Reichmanis, E. Microfluidic Crystal Engineering of pi-Conjugated Polymers. *ACS Nano* **2015**, *9* (8), 8220–8230.
- (102) Chang, M.; Choi, D.; Egap, E. Macroscopic Alignment of One-Dimensional Conjugated Polymer Nanocrystallites for High-Mobility Organic Field-Effect Transistors. *ACS Appl. Mater. Interfaces* **2016**, *8* (21), 13484–13491.
- (103) Wu, D. W.; Kaplan, M.; Ro, H. W.; Engmann, S.; Fischer, D. A.; DeLongchamp, D. M.; Richter, L. J.; Gann, E.; Thomsen, L.; McNeill, C. R.; Zhang, X. R. Blade Coating Aligned, High-Performance, Semiconducting-Polymer Transistors. *Chem. Mater.* **2018**, 30 (6), 1924–1936.
- (104) Persson, N. E.; Engmann, S.; Richter, L. J.; DeLongchamp, D. M. In Situ Observation of Alignment Templating by Seed Crystals in Highly Anisotropic Polymer Transistors. *Chem. Mater.* **2019**, *31* (11), 4133–4147.
- (105) Kim, B. G.; Jeong, E. J.; Chung, J. W.; Seo, S.; Koo, B.; Kim, J. S. A molecular design principle of lyotropic liquid-crystalline conjugated polymers with directed alignment capability for plastic electronics. *Nat. Mater.* **2013**, *12* (7), 659–664.
- (106) Trefz, D.; Gross, Y. M.; Dingler, C.; Tkachov, R.; Hamidi-Sakr, A.; Kiriy, A.; McNeill, C. R.; Brinkmann, M.; Ludwigs, S. Tuning Orientational Order of Highly Aggregating P(NDI2OD-T-2) by Solvent Vapor Annealing and Blade Coating. *Macromolecules* **2019**, *52* (1), 43–54.
- (107) Qu, G.; Zhao, X. K.; Newbloom, G. M.; Zhang, F. J.; Mohammadi, E.; Strzalka, J. W.; Pozzo, L. D.; Mei, J. G.; Diao, Y. Understanding Interfacial Alignment in Solution Coated Conjugated Polymer Thin Films. ACS Appl. Mater. Interfaces 2017, 9 (33), 27863–27874.
- (108) Kim, D. H.; Park, Y. D.; Jang, Y. S.; Yang, H. C.; Kim, Y. H.; Han, J. I.; Moon, D. G.; Park, S. J.; Chang, T. Y.; Chang, C. W.; Joo, M. K.; Ryu, C. Y.; Cho, K. W. Enhancement of field-effect mobility due to surface-mediated molecular ordering in regioregular polythiophene thin film transistors. *Adv. Funct. Mater.* **2005**, *15* (1), 77–82
- (109) Kim, D. H.; Lee, H. S.; Shin, H. J.; Bae, Y. S.; Lee, K. H.; Kim, S. W.; Choi, D.; Choi, J. Y. Graphene surface induced specific self-assembly of poly(3-hexylthiophene) for nanohybrid optoelectronics: from first-principles calculation to experimental characterizations. *Soft Matter* **2013**, *9* (22), 5355–5360.
- (110) Chabinyc, M. L.; Lujan, R.; Endicott, F.; Toney, M. F.; McCulloch, I.; Heeney, M. Effects of the surface roughness of plastic-compatible inorganic dielectrics on polymeric thin film transistors. *Appl. Phys. Lett.* **2007**, *90* (23), 233508.

- (111) Jung, Y.; Kline, R. J.; Fischer, D. A.; Lin, E. K.; Heeney, M.; McCulloch, I.; DeLongchamp, D. M. The effect of interfacial roughness on the thin film morphology and charge transport of high-performance polythiophenes. *Adv. Funct. Mater.* **2008**, *18* (5), 742–750.
- (112) Muller, C.; Aghamohammadi, M.; Himmelberger, S.; Sonar, P.; Garriga, M.; Salleo, A.; Campoy-Quiles, M. One-Step Macroscopic Alignment of Conjugated Polymer Systems by Epitaxial Crystallization during Spin-Coating. *Adv. Funct. Mater.* **2013**, 23 (19), 2368–2377
- (113) Guo, D. Y.; Tsai, Y. B.; Yu, T. F.; Lee, W. Y. Interfacial effects on solution-sheared thin-film transistors. *J. Mater. Chem. C* **2018**, 6 (44), 12006–12015.
- (114) Zhang, F. J.; Mohammadi, E.; Luo, X. Y.; Strzalka, J.; Mei, J. G.; Diao, Y. Critical Role of Surface Energy in Guiding Crystallization of Solution Coated Conjugated Polymer Thin Films. *Langmuir* **2018**, 34 (3), 1109–1122.
- (115) Lee, S. S.; Tang, S. B.; Smilgies, D. M.; Woll, A. R.; Loth, M. A.; Mativetsky, J. M.; Anthony, J. E.; Loo, Y. L. Guiding Crystallization around Bends and Sharp Corners. *Adv. Mater.* **2012**, 24 (20), 2692–2698.
- (116) Kafle, P.; Zhang, F. J.; Schorr, N. B.; Huang, K. Y.; Rodriguez-Lopez, J.; Diao, Y. Printing 2D Conjugated Polymer Monolayers and Their Distinct Electronic Properties. *Adv. Funct. Mater.* **2020**, 30 (12), 1909787.
- (117) Zhang, F. J.; Mohammadi, E.; Qu, G.; Dai, X. J.; Diao, Y. Orientation-Dependent Host-Dopant Interactions for Manipulating Charge Transport in Conjugated Polymers. *Adv. Mater.* **2020**, *32*, 2002823.
- (118) Yang, Y. T.; Liu, Z. T.; Chen, J. M.; Cai, Z. X.; Wang, Z. J.; Chen, W.; Zhang, G. X.; Zhang, X. S.; Chi, L. F.; Zhang, D. Q. A Facile Approach to Improve Interchain Packing Order and Charge Mobilities by Self-Assembly of Conjugated Polymers on Water. *Adv. Sci.* **2018**, *5* (11), 1801497.
- (119) Noh, J.; Jeong, S.; Lee, J. Y. Ultrafast formation of air-processable and high-quality polymer films on an aqueous substrate. *Nat. Commun.* **2016**, *7*, 12374.
- (120) Pandey, M.; Pandey, S. S.; Nagamatsu, S.; Hayase, S.; Takashima, W. Solvent driven performance in thin floating-films of PBITT for organic field effect transistor: Role of macroscopic orientation. *Org. Electron.* **2017**, *43*, 240–246.
- (121) Tripathi, A. S. M.; Pandey, M.; Sadakata, S.; Nagamatsu, S.; Takashima, W.; Hayase, S.; Pandey, S. S. Anisotropic charge transport in highly oriented films of semiconducting polymer prepared by ribbon-shaped floating film. *Appl. Phys. Lett.* **2018**, *112* (12), 123301.
- (122) Soeda, J.; Matsui, H.; Okamoto, T.; Osaka, I.; Takimiya, K.; Takeya, J. Highly Oriented Polymer Semiconductor Films Compressed at the Surface of Ionic Liquids for High-Performance Polymeric Organic Field-Effect Transistors. *Adv. Mater.* **2014**, *26* (37), 6430–6435.
- (123) Gu, X. D.; Shaw, L.; Gu, K.; Toney, M. F.; Bao, Z. N. The meniscus-guided deposition of semiconducting polymers. *Nat. Commun.* **2018**, *9*, 534.
- (124) Blundell, D. J.; Keller, A.; Kovacs, A. J. A new Self-Nucleation Phenomenon and Its Application to the Growing of Polymer Crystals from Solution. *J. Polym. Sci., Part B: Polym. Lett.* **1966**, 4 (7), 481–486.
- (125) Pan, G. X.; Chen, F.; Hu, L.; Zhang, K. J.; Dai, J. M.; Zhang, F. P. Effective Controlling of Film Texture and Carrier Transport of a High-Performance Polymeric Semiconductor by Magnetic Alignment. *Adv. Funct. Mater.* **2015**, 25 (32), 5126–5133.
- (126) Luzio, A.; Criante, L.; D'Innocenzo, V.; Caironi, M. Control of charge transport in a semiconducting copolymer by solvent-induced long-range order. *Sci. Rep.* **2013**, *3*, 3425.
- (127) Choi, D.; Chang, M.; Reichmanis, E. Controlled Assembly of Poly(3-hexylthiophene): Managing the Disorder to Order Transition on the Nano-through Meso-Scales. *Adv. Funct. Mater.* **2015**, 25 (6), 920–927.

- (128) Li, M. M.; An, C. B.; Marszalek, T.; Baumgarten, M.; Yan, H.; Müllen, K.; Pisula, W. Controlling the Surface Organization of Conjugated Donor-Acceptor Polymers by their Aggregation in Solution. *Adv. Mater.* **2016**, 28 (42), 9430–9438.
- (129) Zheng, Y. Q.; Yao, Z. F.; Lei, T.; Dou, J. H.; Yang, C. Y.; Zou, L.; Meng, X. Y.; Ma, W.; Wang, J. Y.; Pei, J. Unraveling the Solution-State Supramolecular Structures of Donor-Acceptor Polymers and their Influence on Solid-State Morphology and Charge-Transport Properties. *Adv. Mater.* **2017**, *29* (42), 1701072.
- (130) Gross, Y. M.; Trefz, D.; Tkachov, R.; Untilova, V.; Brinkmann, M.; Schulz, G. L.; Ludwigs, S. Tuning Aggregation by Regioregularity for High-Performance n-Type P(NDI2OD-T-2) Donor-Acceptor Copolymers. *Macromolecules* **2017**, *50* (14), 5353–5366.
- (131) Matsidik, R.; Luzio, A.; Askin, O.; Fazzi, D.; Sepe, A.; Steiner, U.; Komber, H.; Caironi, M.; Sommer, M. Highly Planarized Naphthalene Diimide-Bifuran Copolymers with Unexpected Charge Transport Performance. *Chem. Mater.* **2017**, *29* (13), 5473–5483.
- (132) Ziffer, M. E.; Jo, S. B.; Liu, Y.; Zhong, H. L.; Mohammed, J. C.; Harrison, J. S.; Jen, A. K. Y.; Ginger, D. S. Tuning H- and J-Aggregate Behavior in, pi-Conjugated Polymers via Noncovalent Interactions. *J. Phys. Chem. C* **2018**, 122 (33), 18860–18869.
- (133) Chu, P. H.; Kleinhenz, N.; Persson, N.; McBride, M.; Hernandez, J. L.; Fu, B. Y.; Zhang, G. Y.; Reichmanis, E. Toward Precision Control of Nanofiber Orientation in Conjugated Polymer Thin Films: Impact on Charge Transport. *Chem. Mater.* **2016**, 28 (24), 9099–9109.
- (134) Yao, Z. F.; Zheng, Y. Q.; Li, Q. Y.; Lei, T.; Zhang, S.; Zou, L.; Liu, H. Y.; Dou, J. H.; Lu, Y.; Wang, J. Y.; Gu, X. D.; Pei, J. Wafer-Scale Fabrication of High-Performance n-Type Polymer Monolayer Transistors Using a Multi-Level Self-Assembly Strategy. *Adv. Mater.* **2019**, *31* (7), 1806747.
- (135) Nahid, M. M.; Welford, A.; Gann, E.; Thomsen, L.; Sharma, K. P.; McNeill, C. R. Nature and Extent of Solution Aggregation Determines the Performance of P(NDI2OD-T2) Thin-Film Transistors. *Adv. Electron Mater.* **2018**, 4 (4), 1700559.
- (136) Takacs, C. J.; Treat, N. D.; Kramer, S.; Chen, Z. H.; Facchetti, A.; Chabinyc, M. L.; Heeger, A. J. Remarkable Order of a High-Performance Polymer. *Nano Lett.* **2013**, *13* (6), 2522–2527.
- (137) Onsager, L. The Effects of Shape on the Interaction of Colloidal Particles. *Ann. N. Y. Acad. Sci.* **1949**, *51* (4), 627–659.
- (138) Bolhuis, P.; Frenkel, D. Tracing the phase boundaries of hard spherocylinders. *J. Chem. Phys.* **1997**, *106* (2), *666*–687.
- (139) Kuriabova, T.; Betterton, M. D.; Glaser, M. A. Linear aggregation and liquid-crystalline order: comparison of Monte Carlo simulation and analytic theory. *J. Mater. Chem.* **2010**, 20 (46), 10366–10383.
- (140) Skoulios, A.; Guillon, D. Amphiphilic Character and Liquid Crystallinity. *Mol. Cryst. Liq. Cryst.* **1988**, *165*, 317–332.
- (141) Khokhlov, A. R.; Semenov, A. N. Liquid-Crystalline Ordering in the Solution of Long Persistent Chains. *Phys. A* **1981**, *108* (2–3), 546–556
- (142) Khokhlov, A. R.; Semenov, A. N. Liquid-Crystalline Ordering in the Solution of Partially Flexible Macromolecules. *Phys. A* **1982**, 112 (3), 605–614.
- (143) Zhang, W. L.; Gomez, E. D.; Milner, S. T. Predicting Nematic Phases of Semiflexible Polymers. *Macromolecules* **2015**, *48* (5), 1454–1462
- (144) Sirringhaus, H.; Wilson, R. J.; Friend, R. H.; Inbasekaran, M.; Wu, W.; Woo, E. P.; Grell, M.; Bradley, D. D. C. Mobility enhancement in conjugated polymer field-effect transistors through chain alignment in a liquid-crystalline phase. *Appl. Phys. Lett.* **2000**, 77 (3), 406–408.
- (145) Zheng, Z. J.; Yim, K. H.; Saifullah, M. S. M.; Welland, M. E.; Friend, R. H.; Kim, J. S.; Huck, W. T. S. Uniaxial alignment of liquid-crystalline conjugated polymers by nanoconfinement. *Nano Lett.* **2007**, *7* (4), 987–992.
- (146) Zhao, N.; Botton, G. A.; Zhu, S. P.; Duft, A.; Ong, B. S.; Wu, Y. L.; Liu, P. Microscopic studies on liquid crystal poly(3,3"-

- dialkylquaterthiophene) semiconductor. *Macromolecules* **2004**, 37 (22), 8307–8312.
- (147) McCulloch, I.; Heeney, M.; Bailey, C.; Genevicius, K.; MacDonald, I.; Shkunov, M.; Sparrowe, D.; Tierney, S.; Wagner, R.; Zhang, W.; Chabinyc, M. L.; Kline, R. J.; McGehee, M. D.; Toney, M. F. Liquid-crystalline semiconducting polymers with high charge-carrier mobility. *Nat. Mater.* **2006**, *S* (4), 328–333.
- (148) DeLongchamp, D. M.; Kline, R. J.; Jung, Y.; Germack, D. S.; Lin, E. K.; Moad, A. J.; Richter, L. J.; Toney, M. F.; Heeney, M.; McCulloch, I. Controlling the Orientation of Terraced Nanoscale "Ribbons" of a Poly(thiophene) Semiconductor. ACS Nano 2009, 3 (4), 780–787.
- (149) Qu, G.; Park, K. S.; Kafle, P.; Zhang, F. J.; Kwok, J. J.; Patel, B. B.; Smilgies, D. M.; Thomsen, L.; McNeill, C. R.; Diao, Y. Lyotropic Liquid Crystalline Mesophase Governs Interfacial Molecular Orientation of Conjugated Polymer Thin Films. *Chem. Mater.* **2020**, 32 (14), 6043–6054.
- (150) Dozov, I. On the spontaneous symmetry breaking in the mesophases of achiral banana-shaped molecules. *Europhys. Lett.* **2001**, 56 (2), 247–253.
- (151) Yang, Y.; Pei, H. W.; Chen, G. D.; Webb, K. T.; Martinez-Miranda, L. J.; Lloyd, I. K.; Lu, Z. Y.; Liu, K.; Nie, Z. H. Phase behaviors of colloidal analogs of bent-core liquid crystals. *Sci. Adv.* **2018**, *4* (5), eaas8829.
- (152) Mandle, R. J.; Goodby, J. W. Progression from nano to macro science in soft matter systems: dimers to trimers and oligomers in twist-bend liquid crystals. *RSC Adv.* **2016**, *6* (41), 34885–34893.
- (153) Bridges, C. R.; Ford, M. J.; Popere, B. C.; Bazan, G. C.; Segalman, R. A. Formation and Structure of Lyotropic Liquid Crystalline Mesophases in Donor-Acceptor Semiconducting Polymers. *Macromolecules* **2016**, *49* (19), 7220–7229.
- (154) Chung, K.; Yang, D. S.; Sul, W. H.; Kim, B. G.; Kim, J.; Jang, G.; Kwon, M. S.; Barlog, M.; Lee, T. S.; Park, S. Y.; Al-Hashimi, M.; Kim, J. Molecular Design Approach for Directed Alignment of Conjugated Polymers. *Macromolecules* **2019**, *52* (17), 6485–6494.
- (155) Cao, X.; Zhao, K.; Chen, L.; Liu, J.; Han, Y. Conjugated polymer single crystals and nanowires. *Polymer Crystallization* **2019**, *2*, e10064.
- (156) Yao, Y. F.; Dong, H. L.; Liu, F.; Russell, T. P.; Hu, W. P. Approaching Intra- and Interchain Charge Transport of Conjugated Polymers Facilely by Topochemical Polymerized Single Crystals. *Adv. Mater.* **2017**, 29 (29), 1701251.
- (157) Park, K. S.; Cho, B.; Baek, J.; Hwang, J. K.; Lee, H.; Sung, M. M. Single-Crystal Organic Nanowire Electronics by Direct Printing from Molecular Solutions. *Adv. Funct. Mater.* **2013**, 23 (38), 4776–4784.
- (158) Paulsen, B. D.; Tybrandt, K.; Stavrinidou, E.; Rivnay, J. Organic mixed ionic-electronic conductors. *Nat. Mater.* **2020**, *19* (1), 13–26.
- (159) Inal, S.; Rivnay, J.; Suiu, A. O.; Malliaras, G. G.; McCulloch, I. Conjugated Polymers in Bioelectronics. *Acc. Chem. Res.* **2018**, *51* (6), 1368–1376.
- (160) O'Carroll, D. M.; Petoukhoff, C. E.; Kohl, J.; Yu, B. X.; Carter, C. M.; Goodman, S. Conjugated polymer-based photonic nanostructures. *Polym. Chem.* **2013**, *4* (20), 5181–5196.
- (161) Kuenstler, A. S.; Kim, H.; Hayward, R. C. Liquid Crystal Elastomer Waveguide Actuators. *Adv. Mater.* **2019**, *31* (24), 1901216. (162) Epps, T. H., III; O'Reilly, R. K. Block copolymers: controlling nanostructure to generate functional materials synthesis, characterization, and engineering. *Chem. Sci.* **2016**, *7* (3), 1674–1689.
- (163) Skylar-Scott, M. A.; Mueller, J.; Visser, C. W.; Lewis, J. A. Voxelated soft matter via multimaterial multinozzle 3D printing. *Nature* **2019**, *575* (7782), 330–335.
- (164) Boley, J. W.; van Rees, W. M.; Lissandrello, C.; Horenstein, M. N.; Truby, R. L.; Kotikian, A.; Lewis, J. A.; Mahadevan, L. Shapeshifting structured lattices via multimaterial 4D printing. *Proc. Natl. Acad. Sci. U. S. A.* **2019**, *116* (42), 20856–20862.
- (165) Patel, B. B.; Walsh, D. J.; Kim, D.; Kwok, J.; Lee, B.; Guironnet, D.; Diao, Y. Tunable structural color of bottlebrush block

copolymers through direct-write 3D printing from solution. Sci. Adv. 2020, 6 (24), eaaz7202.